

# Wind Loaded Structures

---

Alice Alipour, Ph.D., P.E., Iowa State University  
Jay Puckett, Ph.D., P.E., University of Nebraska-  
Lincoln Jeramy Ashlock, Ph.D., Iowa State  
University  
Mahtab Goudarzi, Iowa State University

WisDOT ID

0092-22-06 June

2025



RESEARCH & LIBRARY UNIT



WISCONSIN HIGHWAY RESEARCH PROGRAM

WISCONSIN DOT  
PUTTING RESEARCH TO WORK

## TECHNICAL REPORT DOCUMENTATION PAGE

<b>1. Report No.</b> WisDOT 0092-22-06	<b>2. Government Accession No.</b>	<b>3. Recipient's Catalog No.</b>	
<b>4. Title and Subtitle</b> Wind Loaded Structures		<b>5. Report Date</b> June 2025	
		<b>6. Performing Organization Code</b>	
<b>7. Author(s)</b> Alice Alipour, Jay Puckett, Jeramy Ashlock, Mahtab Goudarzi		<b>8. Performing Organization Report No.</b>	
<b>9. Performing Organization Name and Address</b> Institute for Transportation Iowa State University 2711 South Loop Drive, Suite 4700 Ames, IA 50010-8664  University of Nebraska-Lincoln 1400 R St Lincoln, NE 68588		<b>10. Work Unit No.</b>	
		<b>11. Contract or Grant No.</b> 0092-22-06	
<b>12. Sponsoring Agency Name and Address</b> Wisconsin Department of Transportation Research & Library Unit 4822 Madison Yards Way, Room 911 Madison, WI 53705		<b>13. Type of Report and Period Covered</b> Final Report June 2025	
		<b>14. Sponsoring Agency Code</b>	
<b>15. Supplementary Notes</b>			
<b>16. Abstract</b> Cantilevered traffic sign support structures are subject to wind and truck-induced gusts, which generate torsional and flexural forces that are transferred to their foundations. To standardize the design and construction of these foundations, the Wisconsin Department of Transportation (WisDOT) has developed pre-designed foundation plans.  Focusing on the transmission of moment and torsional forces, this study examined the loads transferred to the foundations of cantilevered traffic sign structures under wind loading conditions. The primary objective was to evaluate whether the current foundation designs are adequate or potentially over-designed.  Two test structures with drilled shaft foundations were subjected to both static and dynamic loading. The investigation analyzed load transfer from the superstructure to the foundations, assessed foundation behavior, and explored opportunities for optimized design. This was accomplished through a combination of geotechnical testing, instrumentation-based data collection, finite element modeling (FEM), and structural health monitoring (SHM).  Model validation was achieved by comparing results from free-vibration and static pull tests with EM outputs. A parametric study further informed the optimization of foundation designs. The results suggest that the current foundation designs, while structurally effective, may include conservative assumptions, particularly in terms of foundation depth, relative to the actual service-level demands observed in testing and modeling. The analysis indicates that it may be possible to reduce foundation depth while still maintaining acceptable performance limits, thereby supporting opportunities for more efficient foundation designs in future practice.			
<b>17. Key Words</b> drilled shaft foundations, load transmission, structural health monitoring, wind-induced traffic sign structure		<b>18. Distribution Statement</b>	
<b>19. Security Classif. (of this report)</b> Unclassified	<b>20. Security Classif. (of this page)</b> Unclassified	<b>21. No. of Pages</b> 57	<b>22. Price</b>

## **DISCLAIMER**

This research was funded through the Wisconsin Highway Research Program by the Wisconsin Department of Transportation and the Federal Highway Administration under Projects 0092-22-06. The contents of this report reflect the views of the authors who are responsible for the facts and accuracy of the data presented herein. The contents do not necessarily reflect the official views of the Wisconsin Department of Transportation or the Federal Highway Administration at the time of publication.

This document is disseminated under the sponsorship of the Department of Transportation in the interest of information exchange. The United States Government assumes no liability for its contents or use thereof. This report does not constitute a standard, specification, or regulation.

The United States Government does not endorse products or manufacturers. Trade and manufacturers' names appear in this report only because they are considered essential to the object of the document.

## TABLE OF CONTENTS

List of Symbols .....	viii
ACKNOWLEDGMENTS .....	x
EXECUTIVE SUMMARY.....	1
1. INTRODUCTION .....	2
1.1 Background.....	2
1.2 Objectives of This Study.....	3
1.3 Structure of the Report.....	3
2. LITERATURE REVIEW .....	5
2.1 Overview.....	5
2.2 Foundation Systems for Sign Structures.....	5
2.3 Torsion and Moment Behavior.....	6
2.3.1 Superstructure .....	6
2.3.2 Drilled Shaft Foundation.....	6
2.4 Instrumentation and Monitoring Technologies .....	8
2.5 Summary of Literature Gaps and Study Relevance .....	9
3. CHARACTERISTICS OF TEST BED STRUCTURES .....	10
3.1 Overview.....	10
3.2 Site-Specific Geotechnical Exploration .....	10
3.3 Superstructure and Shaft Designs .....	12
3.4 Fabrication and Instrumentation of the Structures .....	13
3.4.1 L-Pile and T-Pile Analysis.....	14
3.4.2 Sensor Installation in Shaft .....	17
3.4.3 Strain Gauge Calibration.....	17
3.4.4 Construction of Test Shafts.....	18
3.5 Instrumentation of the Superstructure.....	21
4. TEST RESULTS AND INTERPRETATION .....	23
4.1 Static Test.....	23
4.1.1 Rosette Strain Gauge Data Analysis .....	24
4.1.2 Load Cell Data Analysis .....	27
4.1.3 String Potentiometer Data.....	28
4.2 Foundation Data Analysis .....	31
4.2.1 Filtering of Foundation Strain Gauge Data.....	34
4.2.2 Foundation Strain Gauge Analysis.....	35
4.3 SAP2000 Model.....	36
4.3.1 Modal Analysis .....	39
4.4 Free-Vibration Test.....	39
4.4.1 Acceleration Time History Analysis .....	40

4.5 Summary of Static and Free Vibration Tests.....	41
5. LONG-TERM MONITORING .....	42
5.1 Structural Health Monitoring Data Collection.....	42
5.1.1 Wind Data .....	43
5.2 Acceleration Time History Analysis .....	45
5.3 Data Analysis .....	45
5.3.1 High Wind Analysis .....	47
5.3.2 Structural Response under High Wind for S-13-570 .....	48
5.4 Checking Alternative Foundation Designs .....	49
5.5 Parametric Study Results for Foundation Optimization .....	51
6. CONCLUSIONS.....	54
7. REFERENCES .....	56

## LIST OF FIGURES

Figure 3-1. Location map.....	10
Figure 3-2. Drilled shaft details for S-13-570 and S-13-562 (a) foundation elevation, (b) foundation plan [1].....	12
Figure 3-3. Schematics for (a) S-13-562, and (b) S-13-570 .....	13
Figure 3-4. Deflection of the shaft for S-13-562 .....	15
Figure 3-5. L-Pile analysis for S-13-562: (a) bending moment and (b) shear force distribution along the depth of the shaft.....	15
Figure 3-6. T-Pile torque profile output .....	16
Figure 3-7. Foundation gauges: (a) sensor layout in the foundation elevation and (b) plan for both shafts .....	18
Figure 3-8. Installation of headed bars on the reinforcement cage .....	19
Figure 3-9. Excavation of the hole using excavator-mounted drilling machines.....	19
Figure 3-10 : Placing reinforcement cage for S-13-570.....	20
Figure 3-11: Fixing anchor bars in S-13-570.....	20
Figure 3-12: (a) Structure S-13-562, (b) Structure S-13-570.....	21
Figure 3-13. Instrumentation plan: (a) S-13-562 and (b) S-13-570 .....	22
Figure 3-14. Superstructure instrumentation: (a) accelerometers, (b) string potentiometers for S-13-562, (c) string potentiometers for S-13-570, and (d) pile rosette strain gauges .....	22
Figure 4-1. Static tests on S-13-562: (a) torsional upstream and (b) torsional downstream .....	23
Figure 4-2. Static tests on S-13-570: (a) torsional upstream, (b) torsional downstream, (c) lateral upstream, and (d) lateral downstream.....	24
Figure 4-3. Force components generated by the pulling cable: (a) position of the crane relative to the structure, (b) force components exerted by the cable in downstream torsional tests (horizontal [ $y$ direction] and vertical [ $z$ direction]), and (c) force components exerted by the cable in downstream lateral tests ....	25
Figure 4-4. Angles between rectangular rosette strain gauges.....	26
Figure 4-5. String pots S-13-562: (a) string pot coordinates and (b) global point reference coordinate ....	29
Figure 4-6. String Pots S-13-570: (a) string pot coordinates, (b) global point reference coordinate, and (c) global shaft coordinates .....	29
Figure 4-7. Comparison of bending moments in the $x$ and $y$ directions and torsion between loadcell data and rosette gauge data, torsional downstream test for S-13-570.....	30
Figure 4-8: Translation and rotation at the base, torsional downstream test for S-13-570 .....	30
Figure 4-9. Bending moment from L-Pile analysis.....	33
Figure 4-10. Reliable and unreliable foundation strain gauges: (a) level 1, (b) level 2, (c) level 3, and (d) level 4.....	35
Figure 4-11. Vertical inside strain data before and after filtering in torsional load case, S-13-570.....	36
Figure 4-12. SAP2000 model for S-13-562: (a) two-dimensional view and (b) three-dimensional view ..	38
Figure 4-13. SAP2000 model for S-13-570: (a) two-dimensional view and (b) three-dimensional view ..	38
Figure 4-14. Accelerometers in three directions on both structures.....	40
Figure 5-1: Distribution of data acquisition of the first week of April .....	43
Figure 5-2. Anemometer placement and orientation: (a) standard coordinate system with structural reference, (b) wind direction measurement using anemometer, and (c) alignment of the anemometer's $0^\circ$ reference with standard north.....	44
Figure 5-3. Anemometer installation and reference: (a) anemometer mounted on top of the structure and (b) anemometer manual illustrating wind direction measurement and polar coordinate system.....	44
Figure 5-4: (a) Highest wind event for S-13-562 and (b) highest wind event for S-13-570.....	45
Figure 5-5. Base reaction in S-13-570 for the highest wind: (a) $M_x$ and (b) torsion .....	48
Figure 5-6: L-Pile analysis for highest stochastic wind: (a) S-13-562, and (b) S-13-570 .....	49
Figure 5-7: Top rotations (a) rotation – radius, (b) rotation - shaft depth .....	53
Figure 5-8: Soil translation: (a) translation – radius, (b) translation – shaft depth .....	53

## LIST OF TABLES

Table 3-1. Soil layer $p$ - $y$ curve for S-13-562.....	14
Table 3-2. L-Pile tip load for $p$ - $y$ analysis for S-13-562 .....	14
Table 3-3. Soil layer properties for the structure S-13-562.....	16
<b>Table 3-4. Concrete compressive strength results for S-13-562 .....</b>	<b>21</b>
Table 4-1: Torsional and lateral loading tests setups.....	23
Table 4-2: Static test results – transferred torsional and moment from the superstructure to the base.....	31
Table 4-3: Static test results – rotation and translation at base .....	32
Table 4-4. EA, EI, and GJ of foundation sections.....	32
<b>Table 4-5. Design actions for the foundation with gravity.....</b>	<b>33</b>
Table 4-6. Test actions of foundation S-13-562 .....	33
Table 4-7. Test actions of foundation S-13-570 .....	33
Table 4-8: Table summarizing sensor info shown in Figure 4-10.....	36
Table 4-9. Materials in SAP2000 software .....	37
Table 4-10. Sections in SAP2000 software.....	38
Table 4-11. Natural frequencies based on SAP2000 Model for S-13-562 .....	39
Table 4-12. Natural frequencies based on the SAP2000 Model for S-13-570.....	39
Table 4-13: Summarizing natural frequencies for both structures and all 3 modes in free-vibration test for all acceleration directions .....	40
Table 5-1: Overview of data acquisition .....	42
Table 5-2: Summarizing natural frequencies for both structures and all 3 modes for different acceleration directions.....	46
Table 5-3. Wind coefficients for elements .....	47
Table 5-4. Base reaction of different of stochastic wind model.....	48
Table 5-5. Foundation characteristics of MCIV/TFIV.....	50
Table 5-6. Foundation characteristics of TFII .....	51
Table 5-7: Geometric parameters .....	52
Table 5-8: Soil parameters .....	52
Table 5-9: Load at the top of the shaft .....	52

## List of Symbols

<b>Symbol</b>	<b>Definition</b>	<b>Unit</b>
$V_s$	Velocity of the shear wave	<i>ft/s</i>
$\gamma$	Soil Unit Weight	<i>lb/ft<sup>3</sup></i>
$G_{max}$	Maximum Shear Modulus	<i>Ksi</i>
$X$	Distance in <i>x</i> direction from the base	<i>in.</i>
$Z$	Distance in <i>z</i> direction from the base	<i>in.</i>
$F_{max}$	Maximum Load	<i>k</i>
$\gamma_{xy}$	Shear strain	
$\varepsilon$	Strain	<i><math>\mu\varepsilon</math></i>
$\sigma_x$	Stress in <i>x</i> direction	<i>ksi</i>
$\sigma_y$	Stress in <i>y</i> direction	<i>ksi</i>
EA	Axial Stiffness	<i>k</i>
EI	Flexural Stiffness	<i>k · in<sup>2</sup></i>
GJ	Torsional Stiffness	<i>k · in<sup>2</sup></i>
$\delta$	Logarithmic Decrement	
$\zeta$	Damping Ratio	
$A_n$	Peak of Acceleration Time History at n	
$A_{n+k}$	Peak of Acceleration Time History at k periods after n	
$\mu$	Mean	
$V_{\perp}$	Perpendicular Wind Speed	<i>mph</i>
$V_{\parallel}$	Tangential Wind Speed	<i>mph</i>
$V_g$	Wind Speed	<i>mph</i>
$\theta$	Wind direction	degree
$M_x$	Bending Moment in <i>x</i> direction	<i>k – in</i>
$M_y$	Bending Moment in <i>y</i> direction	<i>k – in</i>
T	Torque	<i>k – in</i>
E	Modulus of Elasticity	<i>ksi</i>
G	Shear Modulus	<i>ksi</i>
$F_y$	Shear	<i>k</i>
$F_z$	Axial Load	<i>k</i>
$M_z$	Torque	<i>k – in</i>
$V_x$	Shear in <i>x</i> direction	<i>k</i>
$V_y$	Shear in <i>y</i> direction	<i>k</i>
$\Delta_x$	Translation in <i>x</i> direction	<i>in.</i>
$\Delta_y$	Translation in <i>y</i> direction	<i>in.</i>
$C_d$	Drag Coefficient	

$k_d$	Directionality Factor	
$k_z$	Height and Expose Factor	
$P_z$	Wind Pressure	<i>ksi</i>
V	Wind Speed	<i>mph</i>
G	Gust Effect Factor	
$I_0$	Moment of Inertia	<i>in.<sup>4</sup></i>
$J_0$	Polar Moment of Inertia	<i>in.<sup>4</sup></i>

## **ACKNOWLEDGMENTS**

This research was funded by grant 0092-22-06 through the Wisconsin Highway Research Program. The research team would like to express their thanks to the efforts of numerous individuals.

The research team is grateful for the in-depth technical review and comments on this research project from the Technical Oversight Committee (TOC) and Project Oversight Committee (POC) Chair Dave Staab / WisDOT, and Steven Doocy / WisDOT, and all TOC members Joe Balice / Federal Highway Administration; Gretchen Bohnhoff / Milwaukee School of Engineering; Scott Breen / Arcadis U.S., Inc.; Kevin Brusso / Jacobs; Michael Dickey / WisDOT; Paulo Florio / WisDOT; Travis Giese / WEMA; Bill Likos / University of Wisconsin – Madison; Hani Titi / University of Wisconsin – Milwaukee; Tri Tran / WisDOT; Andrew Zimmer / WisDOT for their review of the report and feedback. Special thanks go to Technical Support Staff Dr. Dante Fratte and Jamie Valentine and Contract Specialist Shari Kruger.

The researchers also wish to thank Owen Steffens and Martin Case of Iowa State University for leading the efforts for the fabrication and instrumentation of the reinforcement cages in the foundation and superstructures in this project.

## **EXECUTIVE SUMMARY**

Cantilevered traffic sign support structures are regularly exposed to wind and truck-induced gusts, which generate complex torsional and flexural forces that must be effectively transferred to their foundations. These wind-induced stresses, particularly torsional and moment loads, pose significant challenges in design of structure and foundation of such systems. Recognizing the need for consistency and safety, the Wisconsin Department of Transportation (WisDOT) developed standardized foundation plans for these structures. However, questions remain regarding the adequacy and potential conservatism of these designs.

This study investigated the structural behavior and load transfer mechanisms of cantilevered traffic sign structures under wind loading, with a particular focus on the transmission of moment and torsional forces through the foundation system. Two full-span cantilevered truss sign structures with drilled shaft foundations were subjected to both static and dynamic loading to assess performance under realistic operational and environmental conditions.

The research involved geotechnical surveys, finite element modeling (FEM), and structural health monitoring (SHM) to analyze foundation behavior and evaluate torsional capacity. Validation of the computational models was achieved through comparison with experimental results from free-vibration, static pull tests, and long-term monitoring. A parametric study was also conducted to explore opportunities for optimizing foundation design.

Findings indicate that the serviceability limits specified in the WisDOT Bridge Manual may be overly conservative. These results highlight the potential for more efficient foundation designs without compromising structural performance or safety.

# 1. INTRODUCTION

Traffic sign structures are crucial in ensuring safety and facilitating wayfinding in global transportation infrastructures ranging from city roads to rural roads. Traffic sign structures are subjected to various loads, including wind and truck gusts. According to Wisconsin Department of Transportation (WisDOT) Bridge Manual LRFD Standardized Overhead Sign Structure Plans [1] certain traffic sign sizes and types employ standardized foundations developed from conservative soil profiles. Such foundations satisfy safety and performance requirements under varying loading conditions but may be oversized due to these conservative assumptions.

The project aimed to assess the load amplitudes and performance of sign structure foundations under service and wind loads. The focus was on torsion and moment actions under wind loads, how they transfer to foundations, and improved understanding of structural and geotechnical behavior. The research also examined whether the conservative soil assumptions can be refined to improve foundation design efficiency while maintaining structural reliability.

Drilled shafts are designed to resist axial, shear, and bending moments, but torsional moments transmitted into the shaft create specific challenges, particularly in cantilevered sign structures. Torsional resistance remains poorly understood, and additional research is needed to address knowledge gaps. This research attempted to expand understanding of torsional resistance and load transfer mechanisms while providing insights that could lead to more effective foundation design.

## 1.1 Background

Wind loads present significant engineering challenges due to their dynamic, variable, and unpredictable nature. Unlike static loads, wind-induced forces can fluctuate in magnitude, direction, and frequency, making their impact on structures more complex to predict and design for. As the primary components responsible for resisting and transferring these forces to the ground, foundations play a critical role in maintaining the stability and safety of overhead structures, particularly under extreme wind events.

This study specifically focused on two full-span cantilevered truss traffic sign structures. These systems feature long mast arms that extend outward from the support base, forming a pronounced cantilever. This geometry results in substantial torsional stresses being transmitted to the foundation—stresses that are not as prominent in more balanced or symmetric designs. As such, torsional loading becomes a key consideration in the design and evaluation of these structures, underscoring the importance of closely examining foundation behavior under such conditions.

In response to these challenges, the Wisconsin Department of Transportation (WisDOT) developed the *Standardized Overhead Sign Structure Plans* to guide the design and construction of foundations for cantilevered sign structures. However, questions remain regarding whether these standardized designs are overly conservative. Specifically, is there potential overdesign in foundation size or depth, and if so, can they be safely reduced without compromising structural integrity?

To address these questions, this research undertook a comprehensive investigation involving full-scale field testing, structural monitoring, numerical modeling, and a detailed parametric study. The

goal was to evaluate the actual performance of standardized foundations under realistic loading conditions and to determine whether more efficient, yet safe, foundation designs are feasible.

## **1.2 Objectives of This Study**

This project aimed to assess the behavior and extent of loads transferred to two drilled shafts and to evaluate the potential for using smaller-sized drilled shafts to reduce material and construction costs. It was necessary to investigate various aspects of the interaction between the concrete drilled shafts and the soil. WisDOT selected two project sites near Madison, Wisconsin, with comparable wind loads. While the two structures had minor differences, the key differentiator between these structures lay in the soil characteristics at each site, which provided a unique opportunity to examine the impact of soil properties on the load transfer into the foundation.

Static pull tests were conducted to characterize the linear behavior of the structure-foundation system. In these tests, a cable was used to apply controlled loads to the structure. Instrumentation installed captured data during the tests, which were then used for detailed calculations and analysis to understand the response and capacity of the foundation. Structural health monitoring (SHM) was conducted to understand performance under in-service wind loads. Here, sensors continuously monitored the structures' response to wind, temperature fluctuations, and traffic loads. SHM provided real-time data, offering insights into dynamic behavior under normal operating conditions, including strain/stress and displacement variations.

To assess performance under extreme loading conditions, finite element modeling (FEM) was performed using SAP2000 software. This computational approach simulated high wind speeds, transient gusts, and extreme scenarios. FEM allowed for a detailed analysis of stress distribution, structural deformations, and potential failure mechanisms. These simulations were cross-referenced with SHM data to validate the models, ensuring their accuracy and reliability for understanding structural behavior under extreme loads. This approach provided an understanding of how traffic sign structures perform under varying conditions, providing insights into more efficient and reliable designs.

## **1.3 Structure of the Report**

This research report is organized into six chapters, the first of which is this introduction.

Chapter 2 serves as a literature review, summarizing prior research on the responses of traffic sign structures under various loads, with a particular emphasis on torsional effects and a focus on studies involving torsional and lateral loading tests and analysis methods conducted on drilled shafts.

Chapter 3 describes the geotechnical exploration undertaken for this project. It includes detailed accounts of standard penetration tests conducted in the field and soil tests conducted in the laboratory to determine soil stratigraphy. This chapter characterizes the soil conditions that significantly influence the structural responses and capacities of the structures evaluated in subsequent chapters.

Chapter 4 outlines the design, construction, and instrumentation of the superstructure and test shafts. This chapter provides insights into the practical aspects of performing the torsional and lateral tests, corresponding computer models, the free-vibration tests, and details the methodologies employed in preparing the test structures.

Chapter 5 discusses the methods for processing the data recorded during the long-term monitoring. Detailed findings about the torsional response and bending moments experienced by the test shafts under different wind events are included. Furthermore, this chapter compares the estimated torsional capacities of the shafts with existing design standards and policies that govern traffic structure designs, offering an evaluation of current design practices.

Chapter 6 presents the conclusion of this study and summarizes the results.

## **2. LITERATURE REVIEW**

### **2.1 Overview**

Traffic sign structures play a crucial role in regulating movement on highways, roads, and streets worldwide, but wind loading presents significant challenges for their design and performance. Previous research demonstrates that cantilevered traffic sign support structures are frequently employed on highways due to their suitability and economic advantages for shorter spans, providing straightforward installation procedures and reduced material/foundation expenditures [2]. Furthermore, these structures exhibit predictable out-of-plane response characteristics under wind loading conditions and demonstrate less complex dynamic behavior with reduced susceptibility to vibration/gust-induced phenomena compared to long-span configurations [3].

It is important to note that, according to Paiva and Barros [4], cantilevered traffic sign structures must account for multiple loads in addition to structural weight, especially wind loads, which can subject these structures to significant stress. Constantinescu et al. [5] noted that precise wind force calculations for large highway sign structures are important due to possible structural failure under strong wind conditions. In addition, Zuo et al. [6] found that cantilevered mast arm traffic signal supports are prone to significant vibrations in specific wind conditions, causing concerns about structural durability and performance. Tsai and Alipour [7] emphasize the importance of examining wind-induced vibrations in traffic signal structures by conducting long-term monitoring of a traffic signal structure located in Ames, Iowa. Jafari et al. [8] point out the necessity for practical modeling approaches for traffic signal structures that can reduce wind-induced vibration while maintaining structural safety. The studies mentioned above demonstrate that understanding wind effects on traffic sign structures is vital for creating effective design guidelines for these structures. The wind loads manifest themselves within these structures in the form of various inertial loads, including axial, shear, lateral, torsional, and any other combination of loads [7]. Consequently, it is crucial to design and support systems for traffic sign structures under all kinds of loads [9]. This chapter compiles current research and analysis methods on the load response of traffic sign structures and is organized into subject areas that include moment and torsional analysis, dynamic responses, advanced instrumentation, and monitoring techniques.

### **2.2 Foundation Systems for Sign Structures**

In the previous section, studies about the superstructure's response to wind loads were reviewed. It is also important to understand how these loads are transferred to the foundation. Therefore, the stability and performance of traffic sign structures also depend on the behavior of their foundations.

Aguilar Vidal [10] mentioned that the major factor affecting the load response of traffic sign structures is the foundation. Therefore, several studies on different soil and foundation types have been done. According to Barbosa et al. [11] drilled shafts are a popular foundation option for traffic sign structures. South Carolina Department of Transportation (SCDOT) [12] mentioned that drilled shafts are popular due to their high load-bearing capacity, adaptability to different soil conditions, and cost efficiency. Aguilar Vidal [10] noted that the torsional resistance of drilled shafts can be determined by analyzing them under torsional loads. Li et al [13] investigated the torsional capacity of drilled shaft foundations through full-scale instrumented test shafts exposed to quasi-

static monotonic and cyclic torsional loads. In addition, Aguilar Vidal [10] mentioned that the safety factor specified by the Alabama Department of Transportation (ALDOT) for torsional loading might be overly conservative; therefore, by using improved design techniques, it is possible to make precise predictions about the torsional resistance of drilled shafts. Sim et al. [14] offered design guidelines and construction recommendations for incorporation into the Nebraska Department of Transportation (NDOT) regulations, proposing an alternative design for high-mast tower foundations that remove fatigue-prone elements.

Therefore, the foundation is crucial for how traffic sign structures perform. There is a need to understand drilled shaft behavior to create more accurate designs and maintain stability over time.

## **2.3 Torsion and Moment Behavior**

### *2.3.1 Superstructure*

The torsional and moment behavior of traffic sign structures play a critical role in their long-term durability. This section focuses on how natural wind loads affect the superstructure, especially in cantilevered sign structures.

Paiva and Barros [4] demonstrated that cantilever sign structures experience simultaneous gravity and wind loading. Combined loading creates complex stress distributions when structural elements undergo biaxial bending and torsion. Their analysis shows that vertical and horizontal members behave as beam-columns under axial loads, bending moments, and torsional stresses. Understanding torsional and lateral-torsional buckling phenomena is essential for structural stability assessment. Sun et al. [15] used wireless sensor networks to demonstrate a full-scale highway sign structure's behavior over time. The study showed that torsional behavior appears regardless of excitation intensity. Additionally, the structure demonstrates combined bending and torsional behavior, where the primary torsional modes can be detected in vibrations produced by environmental conditions and shaker testing. The authors also emphasized the importance of recording the torsion while looking for damage or changes in real-world sign structures. The American Association of State Highway and Transportation Officials (AASHTO) LRFD Specifications for Structural Supports for Highway Signs, Luminaires, and Traffic Signals [16] establish conservative design pressures based on Finite Element Analysis (FEA) models calibrated through experimental testing. While these pressures provide safety margins across various wind conditions, they may not adequately capture the quasi-static torsional behavior under natural wind where speed and direction fluctuate. In these cases, quasi-static displacements frequently govern structural response. These studies collectively demonstrate that incorporating combined torsional and bending behavior is critical for the design of cantilever sign structures subjected to variable wind conditions.

### *2.3.2 Drilled Shaft Foundation*

Wind-induced Traditional design methods for drilled shaft foundations do not fully account for the complex challenges of wind-induced lateral and torsional loads. These load's interactions with soil conditions and foundation geometry should be understood for accurate and reliable design.

Aguilar Vidal [10] showed that torsional capacity in foundations depends on soil type, loading conditions, and shaft geometry. However, most conventional design approaches overlook torsional loading considerations entirely. The relationship between torsional and overturning resistance is inadequately understood.

Two approaches are commonly used to calculate torsional resistance: the  $\alpha$ -method for clay soils and the  $\beta$ -method for sandy soils. These methods depend on two primary sources of resistance: support from the foundation base and friction between the foundation sides and surrounding soil. Although these methods provide acceptable results, they may not be accurate in all situations because soil properties vary significantly from site to site [10]. Both approaches have limitations. They do not adequately account for shear stress distribution around the foundation perimeter, often leading to overly conservative designs.

Aguilar Vidal [10] observed that combining lateral and torsional loading can increase torsional capacity. However, when lateral loads become eccentric, they reduce overturning resistance. Numerical models show lateral-torsional loading creates complicated failure patterns that start with torsional cracking, develop into large rotational deformations, and eventually complete overturning failure.

Li et al. [13] did experimental testing on two drilled shafts in different soil conditions and revealed significant differences in torsional stress transfer behavior. The shaft with a standard base design exhibited greater torsional resistance due to a thick, silty sand layer near its base. In contrast, the shaft with an engineered frictionless base (using bentonite and plywood layers) demonstrated lower torsional resistance and greater rotation under similar loading conditions. The development of torsional-induced shear cracks in this shaft resulted in higher bending moments and a more flexible lateral response, where lateral loads increased progressively with rotation. Torsional failure in the soil made bending reactions stronger, which shows how complicated the interaction is between lateral and torsional pressures.

Li et al. [17] employed hyperbolic models to obtain the torque-rotation response to gain a more complete understanding of this behavior. These models were able to show how torsional resistance is not linear. A hyperbolic model shows how the torque increases quickly at first with rotation and then slowly reaches a limiting value. This behavior is similar to the soil or structural materials under torsion. In this condition soil or structural materials become less rigid. The results showed that dense sands were significantly harder to twist than clayey silts. The amount of resistance changed depending on the type and depth of soil.

Li et al. [13] used L-Pile and DFSAP models to simulate how lateral loads transfer under combined loading conditions. While these models could predict overall behavior patterns, they missed important effects like lateral load amplification and the softening caused by torsional forces. This limitation indicates that more sophisticated models are necessary to properly account for how torsional and lateral forces interact, particularly in cyclic loading or when soil stiffness varies.

In prior work, three drilled shafts, each with a 3.9-ft. diameter but different lengths were subjected to full-scale tests to assess their combined lateral and torsional responses [18]. Whereas the longer shafts (TS2 and TS3, both 18 ft. in length) primarily failed in torsion with distinct nonlinear lateral responses, the shorter shaft (TS1, 12 ft.) exhibited a hybrid torsion-lateral failure. Unlike the

prediction from the axial load test, torsional resistance decreased by about 20% when stress was combined. The influence of lateral loading and possible residual stress due to prior axial loading were cited as the causes of this decrease.

The linked interaction between these forces was confirmed by the nearly linear decline in the lateral load reduction factor with the torque-to-lateral-load ratio. Analytical torsional resistance was calculated using methods like the  $\alpha$  and  $\beta$  methods, which gave good estimates, with differences from the measured values of up to 14%, with both overestimations and underestimations observed depending on soil conditions and method applied. Cone penetration test (CPT) and standard penetration test (SPT) data-based methods, however, overestimated or underestimated resistance, showing the need for improved methods. To prevent underestimation of the danger of failure, design practice must consider the combined use of torsion and lateral stresses, founded on field observation and numerical analysis [18]. These findings suggest that further investigation of torsion-lateral interaction is essential for developing more precise and less conservative design strategies for drilled shaft foundations.

## **2.4 Instrumentation and Monitoring Technologies**

Previous sections discussed the complicated behavior of traffic sign structures under wind loading. Understanding how these forces change over time is essential for improving the long-term performance of these structures. Pinjan and Zahui [19] developed an approach to address this gap by using polyvinylidene fluoride (PVDF) sensors for real-time structural vibration monitoring. These sensors attach to the structure's surface and capture vibration deflection curves as they happen. From these curves, researchers can determine important physical parameters such as strain, stress, and fatigue life, along with dynamic characteristics like natural frequencies and mode shapes. Pinjan and Zahui [19] validated their approach using a scaled model of a cantilevered stop sign support that replicated the full-scale prototype.

The reliability and precision of the vibration and displacement behavior sensors were established through correlation with accelerometer data. The outcome showed that most of the deformations were found to take place in the bending direction under wind loads, and the details of the structural response were acquired by PVDF sensors. PVDF sensors are a cost-effective and practical tool for continuous monitoring that can be used to monitor and schedule the maintenance of traffic sign structures before any issues occur [19].

The sensors can detect vibrations and bending from the outside; they cannot distinguish what kind of damage happened, such as cracks or corrosion [19]. Also, because PVDF sensors collect real-time data from several sensors, it is necessary to consider storage and data transfer wirelessly when using them on a large scale of infrastructures in the future [15]. In related work, Sun et al. [15] highlighted the importance of using wireless sensor networks (WSNs) for structural health monitoring (SHM) of highway sign structures. These sensors capture natural frequencies and mode shapes, which vibration analysis uses to identify structural damage. Sun et al. placed wireless sensors on a full-scale sign support truss structure and tested a multi-level damage detection approach. The method successfully identified damaged elements under various conditions by analyzing changes in modal properties. The study demonstrates that WSNs improve SHM efficiency that is critical for maintaining traffic sign structures' safety.

## **2.5 Summary of Literature Gaps and Study Relevance**

To summarize the reviewed studies, it is essential to understand the moment and torsional transfer from traffic sign structures to the foundation and torsional resistance of drilled shaft foundations so that they can be designed and optimized for cost savings and safety. Predicting the torsional capacity under different load situations calls for an accurate evaluation of soil properties as well as advanced analytical and numerical methods. Improvements in the efficiency and reliability of traffic sign structures can be achieved by adjusting design safety parameters to reduce soil-specific over-conservatism.

### 3. CHARACTERISTICS OF TEST BED STRUCTURES

#### 3.1 Overview

Two sign structures were instrumented during construction to assess the magnitude and distribution of load transfer along the structures, focusing on the shaft's response to torsion and flexure. This chapter provides a detailed overview of the site characteristics and the design, fabrication, and instrumentation of two traffic sign structures, S-13-562 and S-13-570.

Figure 3-1 illustrates the location map, providing longitude and latitude coordinates of the structures.

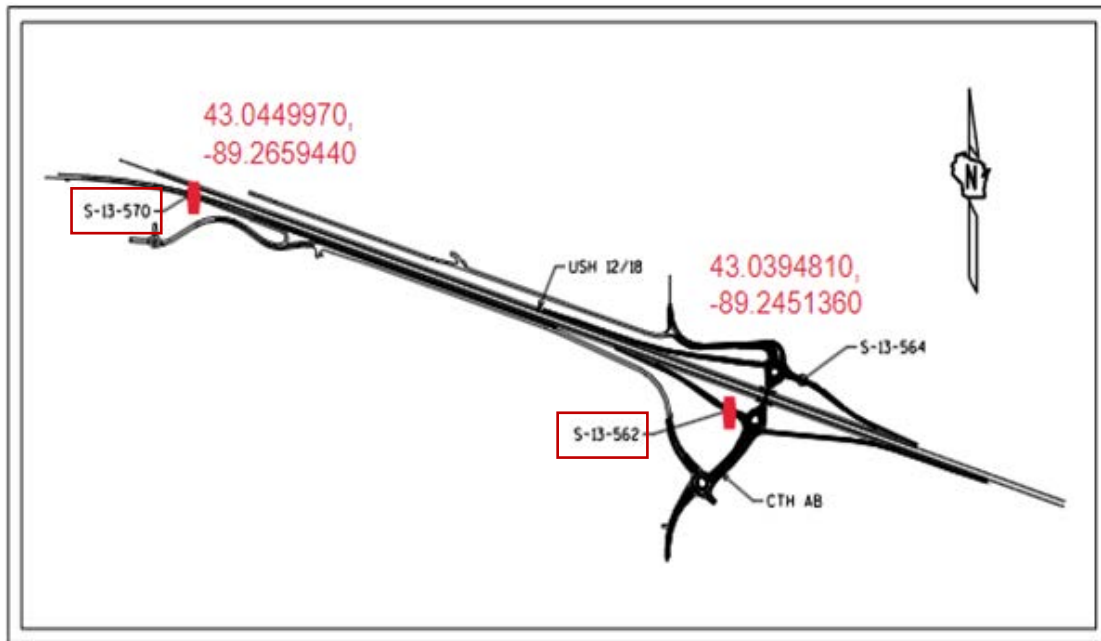


**Figure 3-1. Location map**

#### 3.2 Site-Specific Geotechnical Exploration

On structure S-13-562, a boring log (SB-893-3) was advanced using a 6.25-in. outside-diameter by 2¼-in. inside-diameter hollow-stem auger (HSA) for the entire boring depth. Coring proceeded to a depth of 13.5 ft. using this method, then transitioned to 3-7/8 in. diameter tri-cone rotary coring with 4-in. steel casing and drilling fluid to ensure borehole integrity to terminal depth. SPTs were performed using a standard 2-in. outside-diameter split-barrel sampler at 2.5-ft. intervals in the first 20 ft., followed by 5-ft. intervals up to the termination depth of 30 ft.

The geotechnical profile in boring SB-893-3 consisted of 2.3 ft. of lean clay (CL) fill topsoil followed by 3.2 ft. of lean clay (CL) and measured unconfined compressive strength (UCS) values of 2.5, 3, 1.5, 2.3, 1.8, 2, 2, and 2.4 tsf. Under these layers, there is 2.5 ft. of clayey sand (SC). These were underlain by 4 ft. of silty sand (SM), and then 15 ft. of silty sand with gravel, and cobbles (SM). Following these, there is 14 ft. clayey sand with gravel, and cobbles (SC).

Laboratory analyses, as illustrated in Figure A2 in the Appendix, indicate that the granular fill exhibits moisture contents between 11.6% and 15.3%, and loose to medium dense relative density. The lean clay (CL) strata have stiff to very stiff consistency. The clayey sand (SC) layers have very loose to loose relative density. The silty sand (SM) exhibits medium density. The deeper glacial till formations, comprising silty sand with gravel and cobbles (SM) and clayey sand with gravel and cobbles (SC), present in wet to moist conditions.

The encountered soils exhibited estimated moist unit weights ranging from 120 to 149 pcf. The granular soils demonstrated estimated friction angles between 29 and 36 degrees which are higher than the assumed design value of 24°, and the cohesive soils exhibited an estimated cohesion of 2,000 psf, compared to the assumed 750 psf. These differences suggest that the actual subsurface conditions may provide greater resistance than originally assumed in the design.

Boring log SB-893-3 was a pre-embankment construction boring and therefore does not detail the full as-built soil profile along the site. The final ground surface elevation at the S-13-562 sign location was 901.73 ft. above the elevation on the boring log, with 863.6 ft. of fill placed during construction. It is presumed that the embankment was constructed according to WisDOT standard requirements for embankment construction.

For the S-13-570 structure, one borehole (SB-570-1) was advanced using a 6.25-in. outside-diameter by 2¼-in. inside-diameter hollow-stem auger (HSA) for the entire boring depth. Sampling procedures were consistent with those mentioned in the SB-893-3 boring log.

The soil profile for S-13-570 obtained from Boring SB-570-1 consisted of various layers starting with 4 ft. of a lean clay with sand (CL) fill topsoil having little to no gravel and UCS values of 0.9 and 1.6 tsf. This was underlain by a 2.5-ft. thick black peat (PT) layer with a UCS of 0.5 tsf over a 2.5 ft. lean clay (CL) layer having UCS values of 0.9 and 1.2 tsf, then a 4 ft. layer of fine, poorly graded sand with gravel (SP). Beneath these layers was a 2 ft. layer of lean clay (CL) having UCS values of 1.5 and 0.5 tsf, containing lenses and seams of silt (ML) and fine, poorly graded sand (SP). The deepest layers were glacial tills comprised of a 12-ft. thick layer of silty sand with gravel and cobbles (SM), and finally 3 ft. of clayey sand with gravel and cobbles (SC) extending to the end of the boring.

The laboratory test results, shown in Figure A1 in the Appendix, reveal that the surficial fill topsoil has moisture contents around 40.9%, with medium to stiff consistency. The peat is also moist with very loose to loose relative density. The cohesive strata are moist to wet in moisture content and soft to stiff in consistency. The granular strata are wet to moist, with relative density ranging from loose to medium dense.

The following soil parameters for boring SB-570-1 meet or exceed the values assumed in the shaft design and are noted: Assumed for the purposes of the comparison to the foundation standards that the existing topsoil and peat strata will be removed and be replaced with WisDOT embankment fill material as part of the project construction. The soils encountered are of estimated moist unit weights between 125 and 146 pcf, which are all within the minimum required range. The granular soils have estimated friction angles between 29 and 36 degrees, which is greater than design assumption that is 24°. The cohesive soils have an estimated cohesion of 750 psf, which is the same as design assumption.

The subsurface stratigraphy of the S-13-570 and S-13-562 structures, and lab test results are shown in Figure A1 and Figure A2 in the Appendix.

### 3.3 Superstructure and Shaft Designs

The drilled shafts were designed in accordance with WisDOT specifications for highway and structure construction [1]. According to the LRFD Standardized Structural Plan of WisDOT Bridge Manual [1], the foundation type used for both structures is Two-Chord Cantilever Type IV (TCIV). The diameter associated with the column of the S-13-570 structure corresponds to a drilled shaft diameter of 48 in. based on section 10 of the AASHTO LRFD Bridge Design Specifications [20]. The embedded length of the shaft is 28 ft, according to the WisDOT specification [1]. The required steel reinforcement consists of (14) #10 longitudinal bars and (29) #4 hoops with a minimum 1'-5" hoop lap length [1]. Figure 3-2 illustrates the details of the shafts, the base plate, the anchorage, and the reinforcement. The compressive strength of the concrete for S-13-562 was 5,762 psi on the 7th day after placement and 7,032 psi on the 14th day after placement, that is higher compared to design assumption of 3,500 psi.

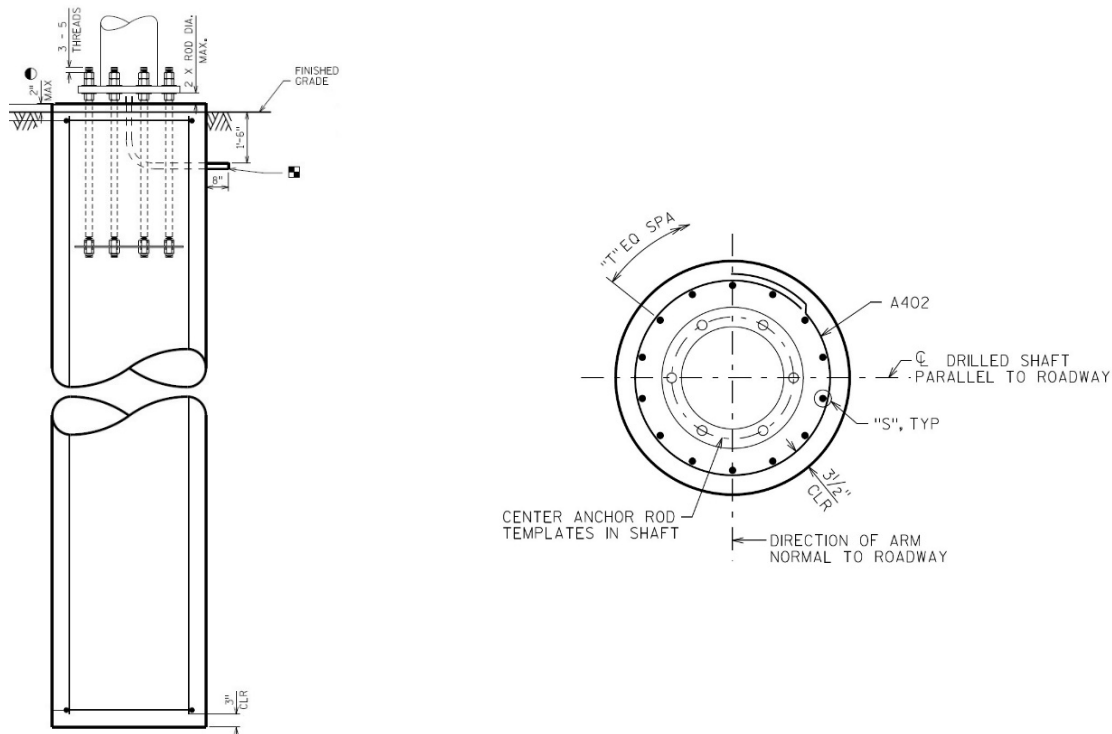


**Figure 3-2. Drilled shaft details for S-13-570 and S-13-562 (a) foundation elevation, (b) foundation plan [1]**

The drilled shafts for S-13-562 and S-13-570 were designed in accordance with AASHTO LRFD Bridge Design Specifications [20] and based on a wind velocity of 115 mph (ultimate). Detailed information on the dimensions of the structures and the materials used is provided below.

Both structures are truss cantilevered sign structures but with different span lengths: S-13-562 is 33 ft. and S-13-570 is 27 ft. Both structures share similar design features, with differences primarily in the span length and sign area. Both structures have a column consisting of 24 in.

diameter pipes made from ASTM A500 Grade C structural steel, with a height of 26'-8" and 27'-9" for S-13-562 and S-13-570, respectively. Both chords are 10-in. diameter pipes made from ASTM A500 Grade C structural steel. The bracing between the mast arms consists of L-shaped members with dimensions of 3 in. × 3 in. × ¼ in., made from ASTM A709 Grade 36 structural steel. Both structures utilize a base plate with a diameter of 36 in. and a thickness of 2 in., fabricated from ASTM A36. The plates are anchored with six bolts, each 2 in. in diameter, made from ASTM F1554 Grade 55. The connection plates measure 33 in. × 26 in. × 2 in. and are made from ASTM A36, with six connection bolts, each 1 in. in diameter, made from ASTM F3125, spaced 29 in. horizontally and 11 in. vertically. The sign area for S-13-562 is 120.50 ft<sup>2</sup>, while the sign area for S-13-570 is 130 ft<sup>2</sup>. Figure 3-3 illustrates the geometries.

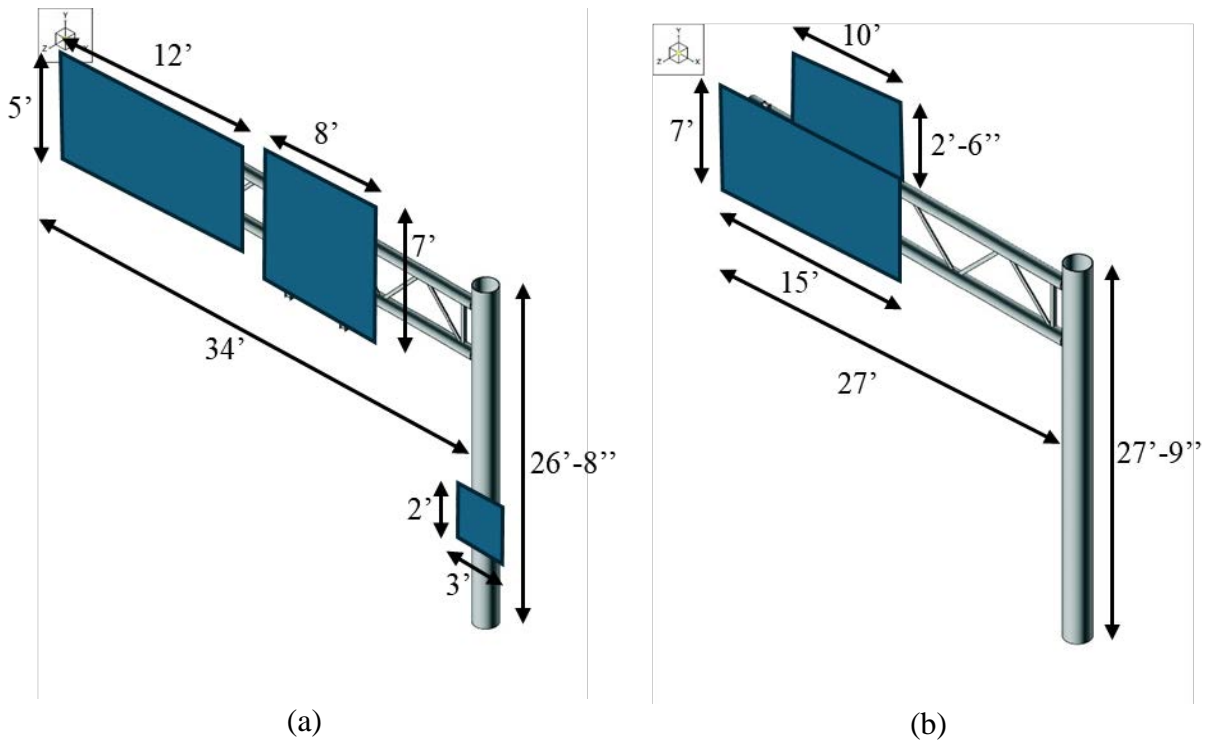


Figure 3-3. Schematics for (a) S-13-562, and (b) S-13-570

### 3.4 Fabrication and Instrumentation of the Structures

The S-13-562 shaft was installed in May 2023, followed by the superstructure construction in June 2023. The S-13-570 shaft was installed in September 2023, and the superstructure was erected in October 2023. The reinforcement cages for the test shafts were built in accordance with the previously described design specifications. In each of the shafts, four longitudinal rebars were left out to allow the research team to install the required instrumentation in controlled conditions and attach the rebars on site. For each steel cage, (14) longitudinal reinforcing bars, each with a length of 27'-7", were fabricated. Additionally, (29) hoops were tied to the longitudinal reinforcing bars. A clear concrete cover of 3.5 in. was maintained.

### 3.4.1 L-Pile and T-Pile Analysis

L-Pile is a software tool used to calculate the deflection, bending moment, and shear forces of a pile by analyzing soil responses along the pile length. The program employs the  $p$ - $y$  method and solves the differential equation using a finite difference approach. While placing more gauges higher in the shaft may provide additional data, the adopted methodology optimally allocated sensors to capture critical variations in response. The use of boring logs reports further strengthens the accuracy of soil characterization, ensuring that the computed pile responses align with actual site conditions. Therefore, the utilized approach provides a balanced and effective monitoring strategy. Therefore, L-Pile utilized the soil information of S-13-562 to determine the optimal sensor locations for capturing the most representative responses of the foundation. Boring log report was used to consider the soil profile of S-13-562 in  $p$ - $y$  analysis. Table 3-1 details the soil layer  $p$ - $y$  curve types. For the first soil layer, the initial plan involved replacing the existing material with WisDOT-approved earthfill, classified and compacted in accordance with Wisconsin Construction Specification 3 – Earthfill [21] which allows select granular soils such as sand (SM, SP) with controlled moisture and compaction conditions.

**Table 3-1. Soil layer  $p$ - $y$  curve for S-13-562**

Layer No.	$p$ - $y$ Curve Type	Topsoil Layer (ft)	Bottom Soil Layer (ft)
1	API <sup>1</sup> Sand (O'Neill [22])	0	2.3
2	API Soft Clay	2.3	5.5
3	API Sand (O'Neill [22])	5.5	8
4	API Sand (O'Neill [22])	8	12
5	API Sand (O'Neill [22])	12	27
6	API Sand (O'Neill [22])	27	28

The tip load data extracted from the structural design report for use in the  $p$ - $y$  analysis is presented in Table 3-2. In this table, " $T$ " represents the torsion at the tip, while " $M$ " denotes the bending moment. Table 3-2 presents the expected loads transferred from the superstructure to the foundation under design conditions.

**Table 3-2. L-Pile tip load for  $p$ - $y$  analysis for S-13-562**

Load Case	Shear (kips)	$M^2$ (k-in.)	Axial (kips)
1	4.5	4398	16.910
2	7.05	1918.8	16.910

The deflection results for structure S-13-562 are provided in Figure 3-4. The maximum deflection of the shaft was estimated as 0.11 in., occurring under loading case 1 (Table 3-2). This result supports placement of the sensors in equal distances along the length of the shaft.

<sup>1</sup> American Petroleum Institute (API)

<sup>2</sup> Bending Moment at top of the drilled shaft

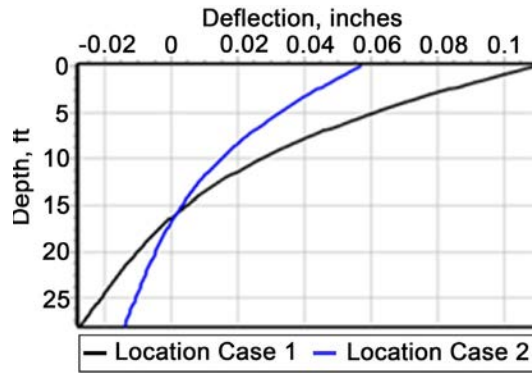


**Figure 3-4. Deflection of the shaft for S-13-562**

The bending moment and shear force distribution results for structure S-13-562 are provided in Figure 3-5.

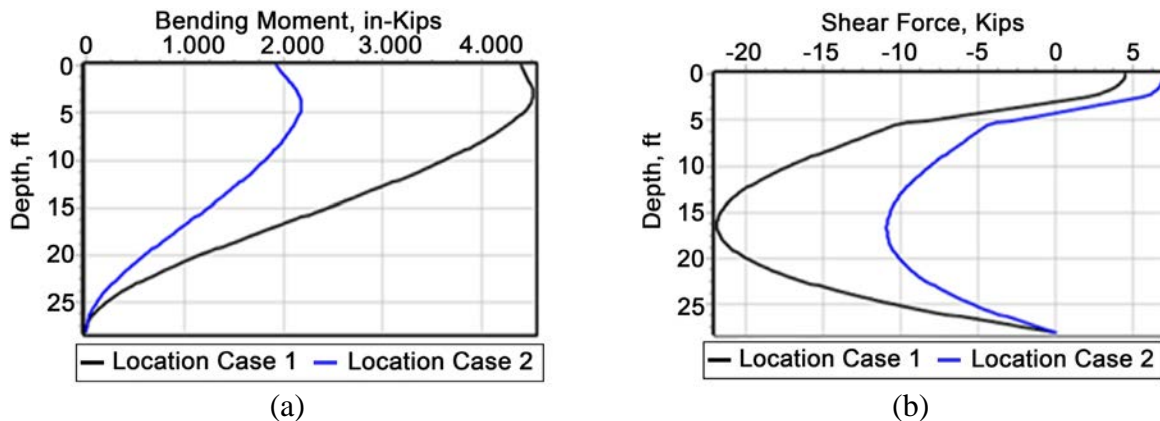


**Figure 3-5. L-Pile analysis for S-13-562: (a) bending moment and (b) shear force distribution along the depth of the shaft**

T-Pile is a software tool used to analyze deep foundations subjected to torsional loads. Understanding torsional behavior is crucial to ensure that ESGs can accurately capture the representative torsional response throughout the foundation’s depth. The T-Pile analysis was conducted using the same set of boring logs utilized in the L-Pile analysis. The soil layer properties are indicated in Table 3-3 for structure S-13-562. In this table, the SPT N-value represents the SPT blow count, which indicates soil resistance by measuring the number of blows required to drive a sampler into 1 ft into the soil. The friction angle defines the shear strength of granular soils, affecting their stability.  $\rho$  represents the density, which influences the load-carrying capacity.  $V_s$  is the velocity of the shear wave, and it is among the most significant parameters in soil stiffness and seismic response evaluation.  $G_{max}$  is the maximum shear modulus, expressing the rigidity of the soil and its resistance against shear deformation.

**Table 3-3. Soil layer properties for the structure S-13-562**

Top of the layer (ft)	Bottom of the layer (ft)	Soil Layer	SPT N-Value (blows/ft)	Friction Angle (°)	$\gamma^3$ (lb/ft <sup>3</sup> )	$V_s^4$ (ft/s)	$G_{max}^5$ (ksi)
0	2.3	Lean Clay (Fill)	7	30	132.42	367.37	3.932
2.3	5.5	Lean Clay	8	0	132.42	391.68	4.469
5.5	8	Clayey Sand	4	29	127.52	378.46	4.017
8	12	Silty Sand	12	33	122.62	543.88	7.978
12	19.5	Silty Sand w/ Gravel and Cobbles	15	30	124.54	585.33	9.395
19.5	27	Silty Sand w/ Gravel and Cobbles	14	34	124.54	572.23	8.972
27	28	Clayey Sand w/ Gravel and Cobbles	9	30	124.54	494.57	6.702

The torque results are presented for S-13-562. The T-Pile analysis revealed that there is no distinct concentration of torsional torque distribution at any specific depth along the shaft. Consequently, the most effective approach to accurately capture the shaft's behavior was to position the ESGs equidistantly along the shaft length, like the placement of the longitudinal strain gauges.

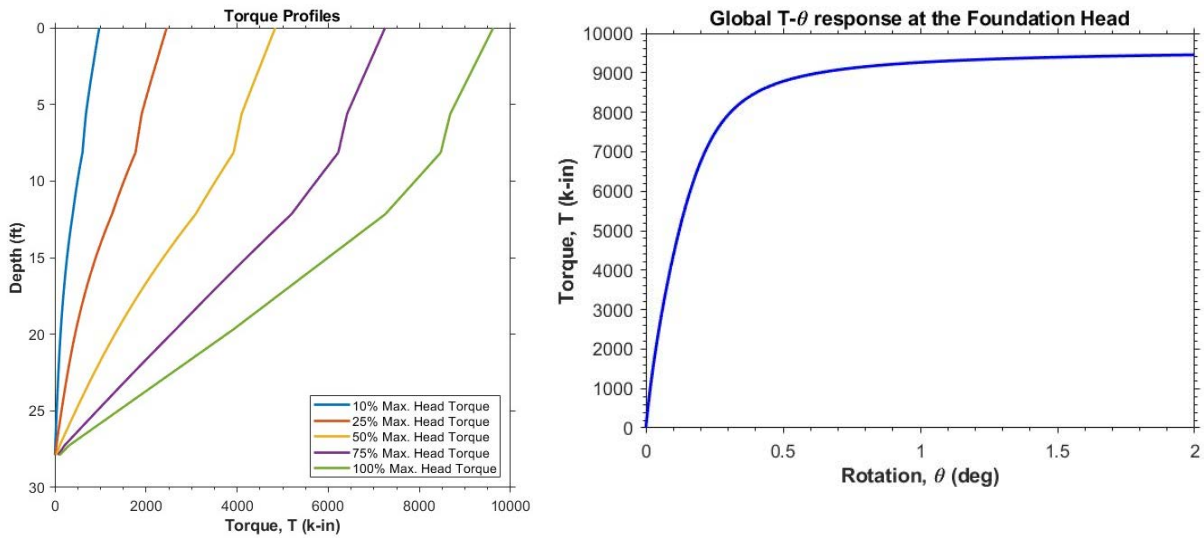


**Figure 3-6. T-Pile torque profile output**

<sup>3</sup> Soil Unit Weight

<sup>4</sup> Shear Wave Velocity

<sup>5</sup> Maximum Shear Modulus

It is important to note that the sensor placement was determined through L-Pile analysis of structure S-13-562. Subsequently, L-Pile analysis was conducted on both structures for foundation design development, as discussed in the following sections.

The stiffness of soil layers affects how well they can resist torsional forces, which changes based on how they may change shape. Materials that are stiffer, like hard clay or sand, resist torsional forces better, which means that torque decreases slowly with depth. Loose sand and soft clay are examples of materials that deform more easily, which makes the torque drop quickly through these layers. This pattern is shown in T-Pile graphs in Figure 3-6. When small torsional force is applied, most of the force goes into the ground's surface. When larger torques are applied, the forces go deeper, therefore more soil layers are needed to stop them.

### 3.4.2 *Sensor Installation in Shaft*

32 strain gauges (16 FLAB-6-350 and 16 FLAB-5-350) were installed on the foundation to monitor strains during static load testing and wind-induced loads. These sensors measure one-dimensional strains on the designated areas, with measurements recorded in micro strains ( $\mu\epsilon$ ). Of the 32 gauges, 16 were placed on the longitudinal rebars to measure longitudinal strains at four different levels. The remaining 16 gauges were mounted on 6.5-in. headed bars and positioned on the reinforcement cage at a 45° angle to measure torsional deformation. These 16 headed bars were placed at the same depth as the longitudinal gauges. Based on the L-Pile and T-Pile analyses for the foundations, the gauges on the reinforcement cage were evenly distributed along the depth at 6'-10" increments. The first level of strain gauges is 4'-8.25" from the head of the shaft. The details are shown in Figure 3-7. The strain gauges were positioned on the inside, outside, downstream, and upstream sides of the shaft at each level. Additionally, RSGs assembled with headed bars were specifically placed on the downstream and upstream sides of the foundation shaft. One headed bar was oriented towards the inside of the structure, while the other was directed towards the outside, with the two bars positioned perpendicular to each other. The headed bars measure strains 45° from the longitudinal axis that are associated with torsional deformations. The layout of the strain gauges is depicted in Figure 3-7, providing a visual representation of their positioning and arrangement. Furthermore, Figure 3-7 also illustrates the shaft reinforcement cage equipped with sensors. To install the RSGs, the surface of the longitudinal bar at the proposed location was first flattened and smoothed using a grinder. After preparing the surface, the RSGs were installed and covered with a protective layer to ensure their durability and functionality. The process of gauge installation is shown in the Appendix.

After installation, the strain gauges were tested to ensure that they were functioning correctly. Figure 3-8 depicts the installation of the headed bars on the reinforcement cage, showing their diagonal positioning.

### 3.4.3 *Strain Gauge Calibration*

The ESGs installed on the headed bars were utilized to measure the torsional deformation. To ensure the reliability of the gauges on the headed bars, they were tested to determine an accurate gauge factor. A rebar testing machine was employed for this purpose. For this purpose, three headed bars were tested, and the corresponding results are presented in the Appendix.

### 3.4.4 Construction of Test Shafts

The foundation construction process started with drilling the shaft holes using an excavator-mounted auger. This part is the same for both structures as illustrated in Figure 3-9. Drilling maintained borehole stability using temporary casing. This technique was not required for any drill slurry. Both sites had groundwater at depths corresponding to the boring logs. Once drilling was completed, the reinforcement cage was placed into the drilled shaft, as shown for S-13-570 as an example in Figure 3-10. Following this, concrete was placed, during which the anchor bars were positioned in the foundation. Concrete was placed using a tremie tube to guarantee continuous placement below the groundwater level and avoid segregation. The concrete placement continued until the foundation was fully completed. The pictures of this process are depicted in the Appendix.

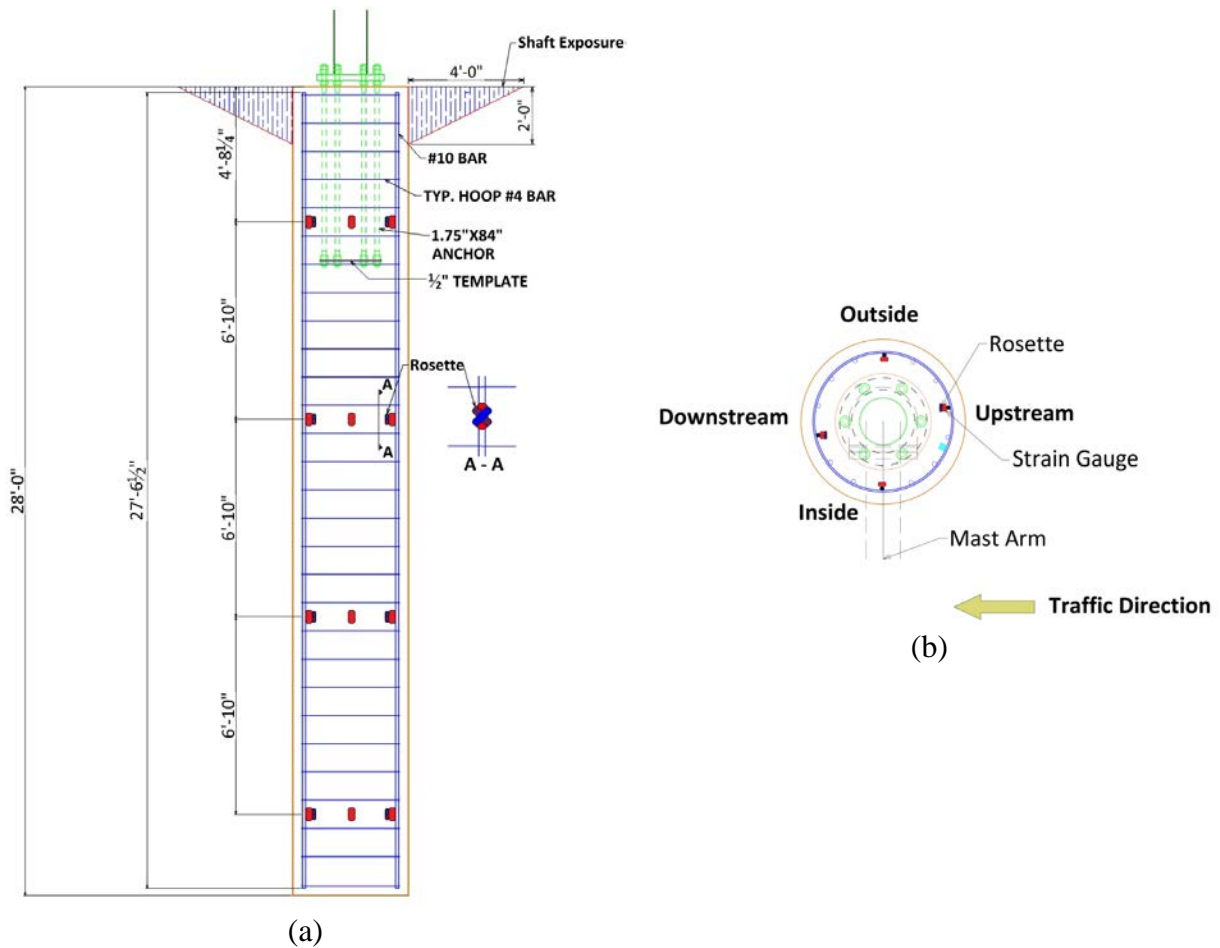


**Figure 3-7. Foundation gauges: (a) sensor layout in the foundation elevation and (b) plan for both shafts**



**Figure 3-8. Installation of headed bars on the reinforcement cage**



**Figure 3-9. Excavation of the hole using excavator-mounted drilling machines**



**Figure 3-10 : Placing reinforcement cage for S-13-570**



**Figure 3-11: Fixing anchor bars in S-13-570**

#### 3.4.4.1 Concrete Compressive Strength

Six concrete samples were collected for S-13-562 to assess the compressive strength of the concrete. These samples underwent testing on the 7th day and 14th day after placement. The concrete compressive strength test results obtained are presented in Table 3-4.

**Table 3-4. Concrete compressive strength results for S-13-562**

Test Day (After Placement)	Compressive Strength (psi)
7	5,765
14	7,032

### 3.5 Instrumentation of the Superstructure

After the completion of the superstructure construction, as shown in Figure 3-12, the instrumentation was installed on both structures.



(a)



(b)

**Figure 3-12: (a) Structure S-13-562, (b) Structure S-13-570**

The instrumentation installed on both structures includes string potentiometers that were installed temporarily during static or pull tests and then removed for long-term monitoring, rosette strain gauges on the pole, longitudinal strain gauges at the connections between the mast arms and the shaft, accelerometers, and an anemometer. Strain gauges were installed at the mast arm and pole connections for both structures. For the S-13-562 structure, four strain gauges were positioned on each side of the mast arm connection, while for the S-13-570 structure, three strain gauges were placed on three sides of the mast arm connection. The detailed arrangement for both structures is illustrated in Figure 3-13. Three accelerometers were installed at the end of the mast arm to measure acceleration in three directions: vertical, horizontal, and out-of-plane. The anemometer was placed at the top of the pole to capture wind speed and direction in long-term monitoring.

Both structures had rosettes installed 12 in. above the foundation connection, which is half the diameter of the pole section, to avoid any localized load effects. Each side of the pole has a group of three rosette strain gauges (rosette) arranged in a rectangular configuration with 45° angles between them. A rosette has three strain gauges and can establish the total strain state (vertical and horizontal normal, and shear).

The S-13-562 and S-13-570 structures differed in terms of the installation of the string potentiometers. As shown in Figure 3-14 (c) a barrier on the inside of the S-13-570 structure prevented the installation of a string potentiometer on that side. However, three string potentiometers are sufficient to capture the rotation and translation at the structure's base. In contrast, string potentiometers could be installed on all four sides of the S-13-562 structure. As a

result, S-13-570 had string potentiometers on three sides (outside, upstream, and downstream), while S-13-562 had them on all four sides. Figure 3-14 shows the instrumentation installed on the structures.

To monitor the response to in-service wind loads and pull tests, a data acquisition system was set up to capture data at 30 Hz, ensuring high-resolution recording of structural responses during tests.

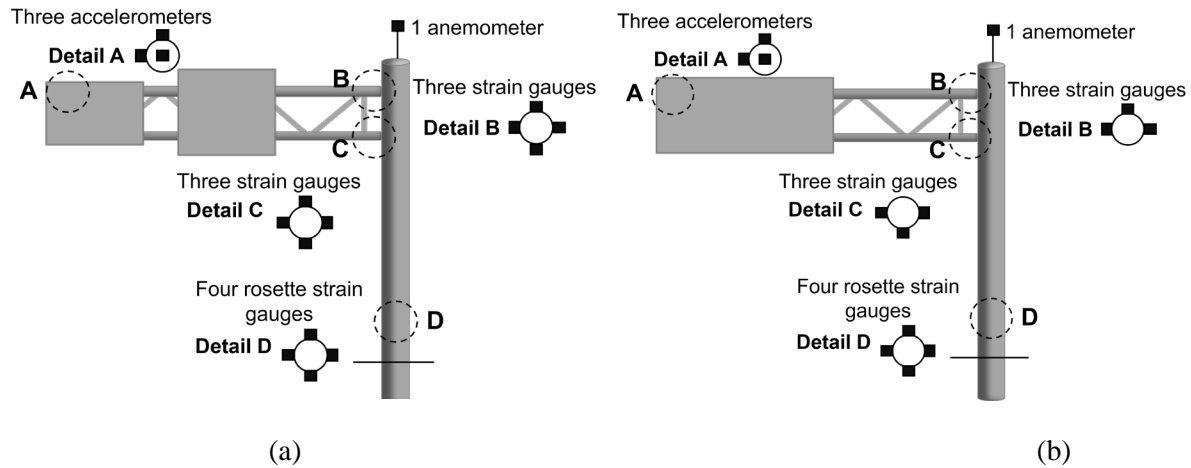


**Figure 3-13. Instrumentation plan: (a) S-13-562 and (b) S-13-570**

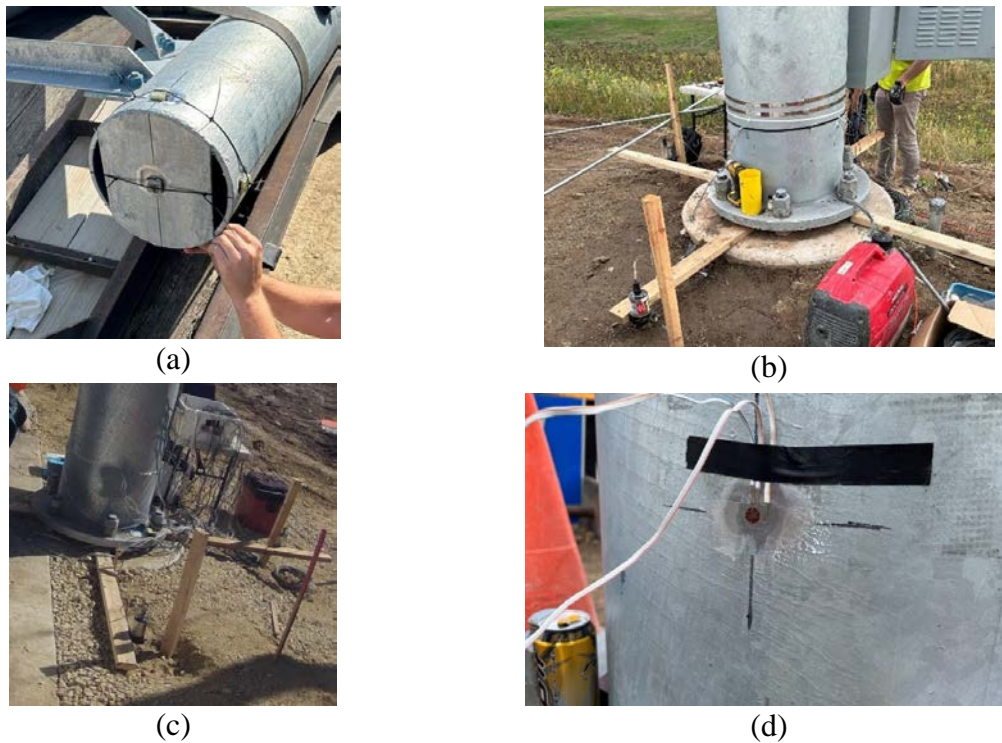


**Figure 3-14. Superstructure instrumentation: (a) accelerometers, (b) string potentiometers for S-13-562, (c) string potentiometers for S-13-570, and (d) pile rosette strain gauges**

## 4. TEST RESULTS AND INTERPRETATION

### 4.1 Static Test

Torsional and lateral loading tests were conducted by applying controlled forces to the structures using a cable that was pulled in two directions, downstream and upstream, as depicted in Figure 4-1 and Figure 4-2 for S-13-562, and S-13-570, respectively. The loadcell was attached to the cable to obtain the load data during pull tests in pounds. The upstream direction refers to the front face of sign panel or approaching side relative to traffic. In contrast, the downstream direction corresponds to the back face of sign panel or departure side relative to traffic. Upstream tests involved pulling the structure toward the upstream side, whereas downstream tests involved pulling it toward the downstream side. The tests began with a target load of 2 kips for torsional loading and 4 kips for lateral loading for S-13-562. The target loads were 7 kips for torsional loading and 5 kips for lateral loading for S-13-570. The torsional and lateral loading test setups including the location of attached cable for both structures are mentioned in Table 4-1.

Data collection was performed at a sampling rate of 30 Hz for both structures to ensure comprehensive coverage from all instruments.

**Table 4-1: Torsional and lateral loading tests setups**

Structure IDs	Torsional Loading Test Setup	Lateral Loading Test Setup
S-13-562	$X^6 = 228$ in. $Z^7 = 285$ in. $F_{max}^8 = 2$ kips	$X = 0$ in. $Z = 285$ in. $F_{max} = 4$ kips
S-13-570	$X = 144$ in. $Z = 285$ in. $F_{max} = 7$ kips	$X = 0$ in. $Z = 285$ in. $F_{max} = 5$ kips



(a)



(b)

**Figure 4-1. Static tests on S-13-562: (a) torsional upstream and (b) torsional downstream**

<sup>6</sup> Distance in x direction from the reference point (base)

<sup>7</sup> Distance in z direction from the reference point (base)

<sup>8</sup> Maximum Load



(a)



(b)



(c)



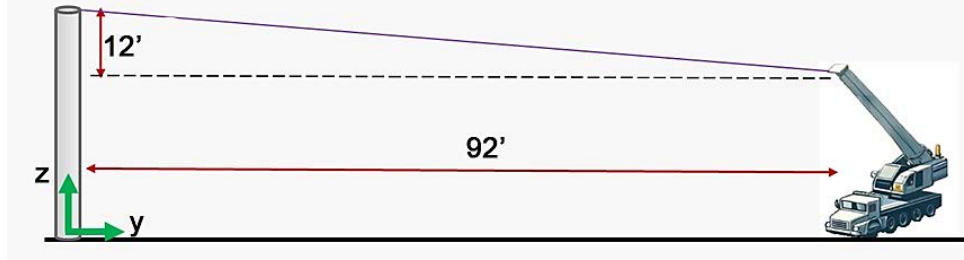
(d)

**Figure 4-2. Static tests on S-13-570: (a) torsional upstream, (b) torsional downstream, (c) lateral upstream, and (d) lateral downstream**

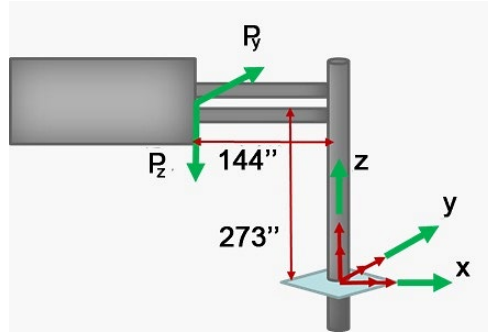
The pulling cable was not completely perpendicular to the mast arm, resulting in an angle between the cable and the horizontal plane. In the torsional tests, the crane was positioned 92 ft. horizontally from the structure, while in the lateral tests it was positioned 83 ft. horizontally from the structure. The vertical distance between the cable attachment point and the highest point of the crane was 12 ft. Based on these configurations, the angle of the cable with the horizontal plane was calculated to be  $8^\circ$ . This angle generated two load components: one in the  $y$ -direction and one in the  $z$ -direction. The illustration of this relative positioning and the resulting loads are identical for both structures and shown in Figure 4-3.

#### 4.1.1 Rosette Strain Gauge Data Analysis

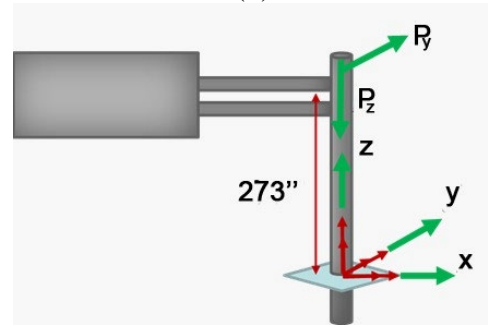
The data from the rosette strain gauges (rosettes) were analyzed to calculate the torsion and bending moments induced by the pulling cable during torsional and lateral loading tests. The equations (4-1), (4-2), and (4-3) were used to determine stresses from strains and to compute the torsion and bending moments in the  $x$  and  $y$  directions.



(a)



(b)



(c)

**Figure 4-3. Force components generated by the pulling cable: (a) position of the crane relative to the structure, (b) force components exerted by the cable in downstream torsional tests (horizontal [y direction] and vertical [z direction]), and (c) force components exerted by the cable in downstream lateral tests**

$$\varepsilon_a = \varepsilon_x \cos^2(\theta_a) + \varepsilon_y \sin^2(\theta_a) + \gamma_{xy} \sin(\theta_a) \cos(\theta_a) \quad (4-1)$$

$$\varepsilon_b = \varepsilon_x \cos^2(\theta_b) + \varepsilon_y \sin^2(\theta_b) + \gamma_{xy} \sin(\theta_b) \cos(\theta_b) \quad (4-2)$$

$$\varepsilon_c = \varepsilon_x \cos^2(\theta_c) + \varepsilon_y \sin^2(\theta_c) + \gamma_{xy} \sin(\theta_c) \cos(\theta_c) \quad (4-3)$$

where,

- $\theta_a$ ,  $\theta_b$ , and  $\theta_c$  were set to  $0^\circ$ ,  $45^\circ$ , and  $90^\circ$ , respectively, based on the arrangement of the rosettes. The angular arrangement of the rosettes is illustrated in Figure 4-4.
- $\varepsilon_a$ ,  $\varepsilon_b$ , and  $\varepsilon_c$  correspond to strains derived from the horizontal, diagonal, and vertical rosettes, respectively.
- $\varepsilon_x$ ,  $\varepsilon_y$ , and  $\gamma_{xy}$ , calculated at each time step, represent the following:

- $\epsilon_x$  represents the tangential strain component on each side of the pole, denoted as  $t$  in polar coordinates.
- $\epsilon_y$  represents the vertical strain component on each side of the pole, denoted as  $z$  in polar coordinates.
- $\gamma_{xy}$  corresponds to the shear strain, equivalent to  $\gamma_{zt}$  in polar coordinates.

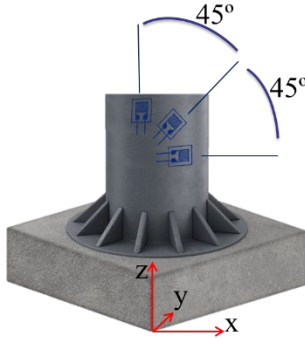


**Figure 4-4. Angles between rectangular rosette strain gauges**

After determining the principal strains from the rosettes, the stresses were calculated using equations (4-4), (4-5), and (4-6). In these calculations, the modulus of elasticity ( $E$ ) was 29,000 ksi, Poisson's ratio ( $\nu$ ) was 0.3, and the shear modulus ( $G$ ) was 11,154 ksi, as determined from equation (4-7).

$$\sigma_x = \frac{E}{1-\nu^2} (\epsilon_x + \nu\epsilon_y) \quad (4-4)$$

$$\sigma_y = \frac{E}{1-\nu^2} (\epsilon_y + \nu\epsilon_x) \quad (4-5)$$

$$\tau_{xy} = \gamma_{xy} G \quad (4-6)$$

$$G = \frac{E}{2(1+\nu)} \quad (4-7)$$

The bending moments and torsion were determined after calculating the tangential and vertical stresses for each side of the pole using data from the rosettes. The bending moment in the  $x$  direction at the base is related to the vertical stresses on the upstream ( $\sigma_{zu}$ ) and downstream ( $\sigma_{zd}$ ) sides, as described in equation (4-8). Similarly, the bending moment at the base in the  $y$  direction is influenced by the vertical stresses on the outside ( $\sigma_{zo}$ ) and inside ( $\sigma_{zi}$ ) faces, as defined in equation (4-9).

$$M_x = \frac{(\sigma_{zd} - \sigma_{zu})I_0}{2 \times r} \quad (4-8)$$

$$M_y = \frac{(\sigma_{zi} - \sigma_{zo})I_0}{2 \times r} \quad (4-9)$$

To calculate torsion, the maximum shear stress ( $\tau_{tz}$ ) from the four sides of the pole, downstream, upstream, inside, and outside, was used, as shown in equation (4-10). These calculations were performed at each step to capture the time history response.

$$T = \frac{\tau_{tz}J_0}{r} \quad (4-10)$$

#### 4.1.2 Load Cell Data Analysis

An analysis of the load cell data is also conducted to ensure the reliability of the data derived from the rosettes. The key aspect is that the stresses and bending moments in the  $x$  and  $y$  directions, calculated from both the rosettes and the load cell data, should be closely aligned. If this alignment is observed, the rosettes are dependable, and the resulting base torsion and bending moment calculations are accurate.

Using the load geometry illustrated in Figure 4-3, equations (4-11), (4-12), and (4-13) are utilized to calculate moments and torsion. In these equations,  $z$  value is 273 in. for torsional and lateral loading tests, representing the distance between the point where the cable is attached to the mast arm and the position of the rosettes, which were located 12 in. (half of the pole diameter) above the base connection in the  $z$  direction. The  $x$  value is 228 in. and 144 in. in torsional loading tests for S-13-562 and S-13-570, respectively. This value was zero in lateral loading tests, representing the distance between the point where the cable was connected and the center of the pole in the  $x$  direction.

$$\sum M_x = F_y \times z \quad (4-11)$$

$$\sum M_y = F_z \times x \quad (4-12)$$

$$\sum M_z = F_y \times x \quad (4-13)$$

The vertical and shear stresses obtained from the loadcell were comparable to those obtained from the rosettes. To calculate these stresses, values for torsion, bending moments, shear forces in the  $x$  and  $y$  directions, and axial load were required. The calculations utilized equations (4-14), (4-15), and (4-16) to determine the shear and axial forces.

$$\sum V_y = F_y - P_y = 0 \Rightarrow F_y = +P_y \text{ lb} \quad (4-14)$$

$$\sum V_x = F_x + 0 = 0 \Rightarrow F_y = 0 \quad (4-15)$$

$$\sum F_z = F_z - P_z = 0 \Rightarrow F_z = +P_z \text{ lb} \quad (4-16)$$

The corresponding shear and normal stresses were determined using equations (4-17) and (4-18).

$$\sigma_z = \pm \frac{M_x r}{I_0} \pm \frac{M_y r}{I_0} + \frac{P_z}{A_0} \quad (4-17)$$

$$\tau_{tz} = \pm \frac{V_x}{A_{shear}} \pm \frac{V_y}{A_{shear}} + \frac{Tr}{J_0} \quad (4-18)$$

### 4.1.3 String Potentiometer Data

The next step involved analyzing the string potentiometer data to calculate the base connection's torsion, rotation, and displacements. S-13-570 and S-13-562 are quite different in terms of the use of string potentiometers. As described above, the barrier at the inside position of S-13-570 did not allow for the installation of a string potentiometer on the interior side of the pole, and therefore only three string potentiometers were used. S-13-562 had no barriers, and four string potentiometers could be used.

Initially, the coordinates from the string potentiometer differed from the global coordinate, as shown in Figure 4-5 and Figure 4-6 for S-13-562 and S-13-570, respectively. In these figures, the orange squares show the placement of the string pots corresponding to the wooden bars. Therefore, the raw string potentiometer data must be converted to the global coordinate system.

For S-13-562, the outside string potentiometers' coordinates were aligned with the global coordinate reference. However, the upstream, downstream, and inside coordinates were not aligned, as shown in Figure 4-5. To align these, the string potentiometer data from these sides needed to be multiplied by -1. All string potentiometer data for S-13-570 were multiplied by -1 to align with the global coordinates.

In equations (4-19), (4-20), (4-21), and (4-22),  $\Delta_{1x}$  represents the translation in the global coordinate system for the upstream side in the  $x$  direction,  $\Delta_{2x}$  represents the translation for the downstream side in the  $x$  direction,  $\Delta_{1y}$  represents the translation for the outside in the  $y$  direction, and  $\Delta_{2y}$  shows the translation for the inside in the  $y$  direction.

$$\Delta_{1x} = -\Delta_1 \quad (4-19)$$

$$\Delta_{2x} = -\Delta_2 \quad (4-20)$$

$$\Delta_{1y} = -\Delta_3 \quad (4-21)$$

$$\Delta_{2y} = -\Delta_4 \quad (4-22)$$

To determine the translations in the  $x$  and  $y$  directions as well as the rotation, equations (4-23) to (4-27) were applied.

$$\Delta_x = \frac{\Delta_{1x} + \Delta_{2x}}{2} \quad (4-23)$$

$$\Delta_y = \frac{\Delta_{3y} + \Delta_{4y}}{2} \quad (4-24)$$

$$\Delta\theta_1 = \frac{\Delta_{3y} - \Delta_{4y}}{l_3 + l_4} \quad (4-25)$$

$$\Delta\theta_2 = \frac{\Delta_{1x} - \Delta_{2x}}{l_1 + l_2} \quad (4-26)$$

$$\Delta\theta = \frac{\Delta\theta_1 + \Delta\theta_2}{2} \quad (4-27)$$

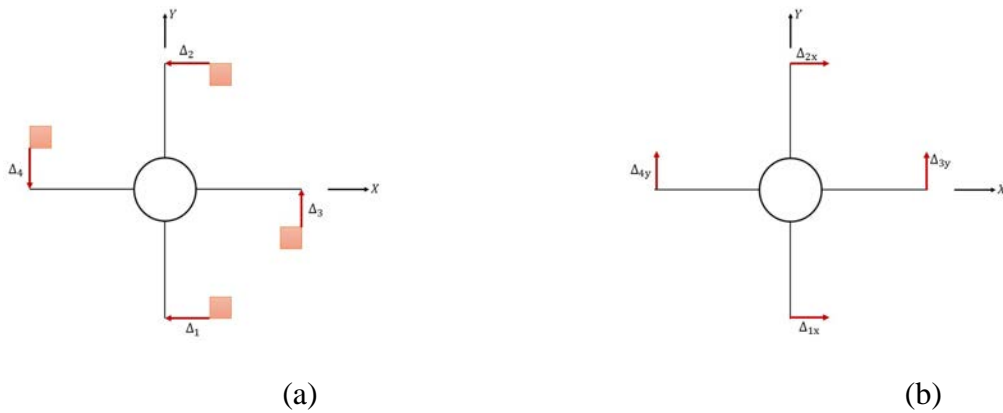


**Figure 4-5. String pots S-13-562: (a) string pot coordinates and (b) global point reference coordinate**

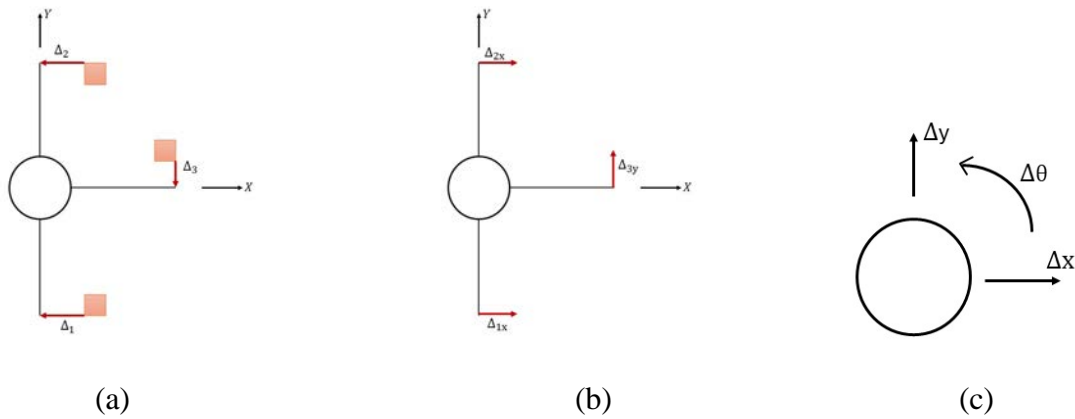


**Figure 4-6. String Pots S-13-570: (a) string pot coordinates, (b) global point reference coordinate, and (c) global shaft coordinates**

Based on these data, translation and rotation were calculated using equations (4-28), (4-29), and (4-30) for S-13-570.

$$\Delta_x = \frac{\Delta_{1x} + \Delta_{2x}}{2} \quad (4-28)$$

$$\Delta_y = (\Delta_{1y} + \theta r_{1y}) \quad (4-29)$$

$$\Delta\theta = \frac{\Delta_{1x} - \Delta_{2x}}{l_1 + l_2} \quad (4-30)$$

The following presents and summarizes the results of the transferred torsional and moment from superstructure to the base connection. The torsional upstream, lateral loading test for S-13-570, lateral and torsional loading test results for S-13-562 are mentioned in the Appendix. Figure 4-7 shows the alignment of torsion and bending moments in the  $x$  and  $y$  directions between the rosette strains and the loadcell data for torsional downstream test for S-13-570.

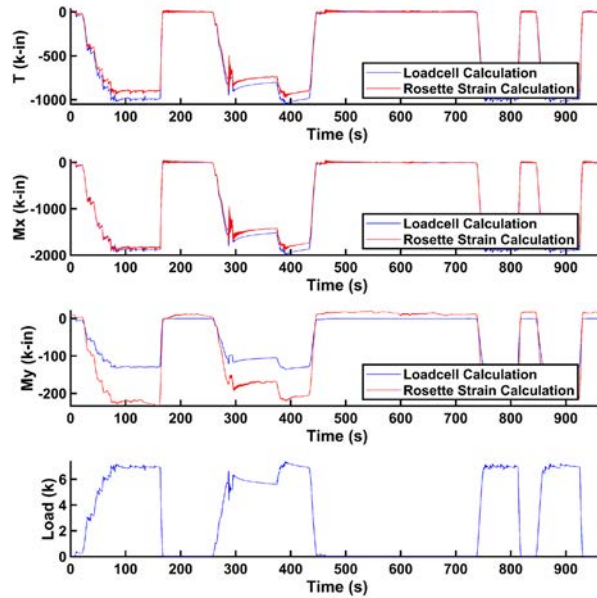


**Figure 4-7. Comparison of bending moments in the  $x$  and  $y$  directions and torsion between loadcell data and rosette gauge data, torsional downstream test for S-13-570**

The comparison between the actual load, derived from the load cell data analysis, and the data from the rosettes confirms a good match. At the base connection, the torsion reached a maximum of approximately 1,200 k-in as shown in Figure 4-7. The bending moment in the  $x$  direction was around 2,000 k-in., corresponding to the applied load in the  $y$  direction. In contrast, the bending moment in the  $y$  direction was significantly smaller, approximately 200 k-in., due to the lower load component in the  $z$  direction. The test results for both structures are mentioned in Table 4-2. Figure 4-8 presents the time histories of translation and rotation in relation to the applied load in the torsional downstream loading test. The test results for both structures are summarized in Table 4-3.

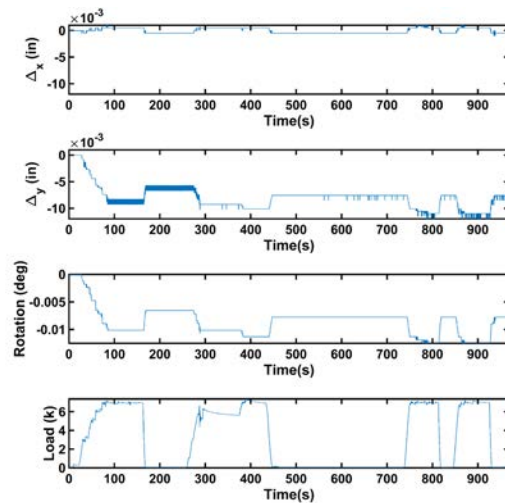


**Figure 4-8: Translation and rotation at the base, torsional downstream test for S-13-570**

**Table 4-2: Static test results – transferred torsional and moment from the superstructure to the base**

	<b>S-13-562</b>	<b>S-13-570</b>
<b>TD<sup>9</sup> - Load (kips)</b>	2	7
<b>TD - <math>M_x</math> (k-in)</b>	600	2000
<b>TD - <math>M_y</math> (k-in)</b>	60	250
<b>TD - T (k-in)</b>	500	1200
<b>TU<sup>10</sup> - Load (kips)</b>	2	7
<b>TU - <math>M_x</math> (k-in)</b>	600	2000
<b>TU - <math>M_y</math> (k-in)</b>	60	80
<b>TU - T (k-in)</b>	500	1200
<b>LD<sup>11</sup> - Load (kips)</b>	4	5
<b>LD - <math>M_x</math> (k-in)</b>	1200	1600
<b>LU<sup>12</sup> - Load (kips)</b>	4	5
<b>LU - <math>M_x</math> (k-in)</b>	1200	1500

#### 4.2 Foundation Data Analysis

The initial step in assessing the foundation’s performance during the tests was to determine whether any cracks were present. Figure 3-7 depicts the foundation, highlighting various sections and the levels at which gauges were installed. Section properties were both computed in SAP2000 and manually calculated. The results obtained from SAP2000 are presented in the Appendix, while the manually calculated section properties are provided in Table 4-4. According to the results, the axial stiffness (EA) was  $4.5 \times 10^6$  kips in the first level and  $4.3 \times 10^6$  kips in the other levels. The flexural stiffness (EI) was  $9.6 \times 10^8$  and  $8.8 \times 10^8 \text{ k} \cdot \text{in}^2$  in the first level and other levels, respectively. The torsional stiffness (GJ) was  $7.39 \times 10^{11}$  and  $6.8 \times 10^{11} \text{ k} \cdot \text{in}^2$  in the first level and other levels, respectively. The difference between the first level and other levels, as shown in Figure 3-7 was the presence of anchor bars in the first level.

---

<sup>9</sup> Torsional Downstream

<sup>10</sup> Torsional Upstream

<sup>11</sup> Lateral Downstream

<sup>12</sup> Lateral Upstream

**Table 4-3: Static test results – rotation and translation at base**

	<b>S-13-562</b>	<b>S-13-570</b>
<b>TD<sup>13</sup> - Load (kips)</b>	2	7
<b>TD - rotation (deg)</b>	0.0006	0.012
<b>TD - <math>\Delta_y</math><sup>14</sup> (in.)</b>	0.002	0.01
<b>TD - <math>\Delta_x</math><sup>15</sup> (in.)</b>	0.0001	0.001
<b>TU<sup>16</sup> - Load (kips)</b>	2	7
<b>TU - rotation (deg)</b>	0.001	0.004
<b>TU - <math>\Delta_y</math> (in.)</b>	0.001	0.0025
<b>TU - <math>\Delta_x</math> (in.)</b>	0.001	0.001
<b>LD<sup>17</sup> - Load (kips)</b>	4	5
<b>LD - <math>\Delta_y</math> (in.)</b>	0.002	0.006
<b>LU<sup>18</sup> - Load (kips)</b>	4	5
<b>LU - <math>\Delta_y</math> (in.)</b>	0.002	0.01

**Table 4-4. EA<sup>19</sup>, EI<sup>20</sup>, and GJ<sup>21</sup> of foundation sections**

	<b>Level 1</b>	<b>Level 2, 3, and 4</b>
<b>EA (kips)</b>	$4.5 \times 10^6$	$4.3 \times 10^6$
<b>EI (<math>k \cdot in^2</math>)</b>	$9.6 \times 10^8$	$8.8 \times 10^8$
<b>GJ (<math>k \cdot in^2</math>)</b>	$7.39 \times 10^{11}$	$6.8 \times 10^{11}$

Based on the section details and the strain gauge installations at different levels, the sections did not crack because the moment of cracking in the sections was a minimum of 5,265 k-in. for the first level and a minimum of 4,831 k-in. for the other levels. Meanwhile, the maximum moments that occurred during the tests on S-13-562 and S-13-570 were 1,200 k-in. and 2,000 k-in., respectively, which were smaller than moment of cracking. The design actions are shown in Table 4-5. The test actions are shown in Table 4-6 and for S-13-562 and S-13-570, respectively. Pull tests were used to calibrate sensor responses and FEM. Actual response data to be used to check foundation adequacy would come from wind measurements.

---

<sup>13</sup> Torsional Downstream

<sup>14</sup> Translation in y direction

<sup>15</sup> Translation in x direction

<sup>16</sup> Torsional Upstream

<sup>17</sup> Lateral Downstream

<sup>18</sup> Lateral Upstream

<sup>19</sup> Axial Stiffness

<sup>20</sup> Flexural Stiffness

<sup>21</sup> Torsional Stiffness

**Table 4-5. Design actions for the foundation with gravity**

Design Actions with Gravity (Top of Shaft)	Units	Value	Test/Design Load
$M_x$ <sup>22</sup> lateral load case	k-in	4,668	0.46
$M_x$ torsional load case	k-in	4,824	0.42
$T_z$ <sup>23</sup> torsional load case	k-in	996	1.0
Computed approximate steel strain/stress at test load (top of shaft)	$\mu$ strain/ksi	52.3 $\mu\epsilon$	1.52 ksi
Computed approximate steel strain/stress at test load (top of shaft)	$\mu$ strain/ksi	54.0 $\mu\epsilon$	1.57 ksi
Computed approximate steel strain/stress at test load (top of shaft)	$\mu$ strain/ksi	11.1 $\mu\epsilon$	0.32 ksi

**Table 4-6. Test actions of foundation S-13-562**

Test Actions (Top of Shaft)	Units	Value	Value/ $M_{crack}$ <sup>24</sup>
$M_x$ lateral load case	k-in	1,200	0.233
$M_x$ torsional load case	k-in	600	0.116
$T_z$ torsional load case	k-in	600	0.116

**Table 4-7. Test actions of foundation S-13-570**

Test Actions (Top of Shaft)	Units	Value	Value/ $M_{crack}$
$M_x$ lateral load case	k-in	1,596	0.310
$M_x$ torsional load case	k-in	2,004	0.389
$T_z$ torsional load case	k-in	996	0.193

The next step involved comparing the expected design actions with the observed test actions. During the design phase, calculations indicated that the  $M_x$  value would be 85% of  $M_{crack}$ , which is the minimum bending moment required to initiate a crack in a concrete section.  $M_y$  would be 61% of  $M_{crack}$ , and the torsional moment would be approximately 50% of  $M_{crack}$ . Furthermore, the L-Pile analysis suggested that the maximum bending moment would occur around 5 ft. (approximately at level 1), with all other levels expected to experience smaller bending moments in comparison. The output bending moment from L-Pile analysis is shown in Figure 4-9.

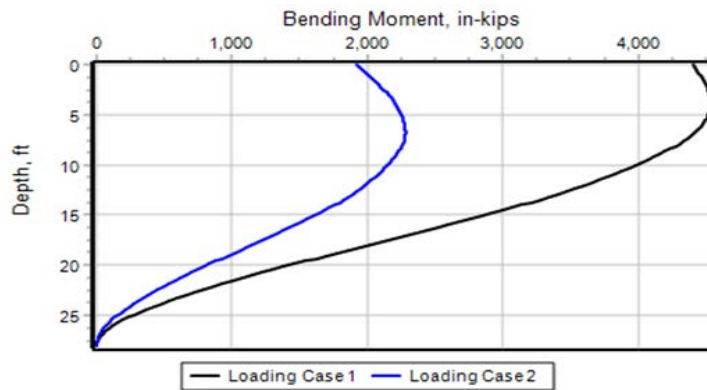


**Figure 4-9. Bending moment from L-Pile analysis**

<sup>22</sup> Bending moment in  $x$  direction

<sup>23</sup> Torsion

<sup>24</sup> Cracking Moment

The pull test results for S-13-562 were as follows: the maximum bending moment ( $M_x$ ), considering moments in both the  $x$  and  $y$  directions, reached 23% of  $M_{crack}$  under the lateral load case. For the torsional load case,  $M_x$  was 11% of  $M_{crack}$ , with torsion accounting for 11% of  $M_{crack}$ .

The pull test results for S-13-570 were as follows: The maximum bending moment ( $M_x$ ), considering moments in both the  $x$  and  $y$  directions, reached 30% of  $M_{crack}$  under the lateral load case. For the torsional load case,  $M_x$  was 40% of  $M_{crack}$ , with torsion accounting for 20% of  $M_{crack}$ .

In summary, the strain data from the tests indicates that the lower gauge readings are minimal, likely dominated by noise. This result was anticipated based on the L-Pile analysis previously presented, and the observed results are consistent with the initial design expectations.

#### 4.2.1 *Filtering of Foundation Strain Gauge Data*

After reviewing the design and test actions, the next step involved processing the data obtained from the foundation gauges to extract the strain corresponding to the applied load at each level. As previously discussed, some gauges malfunctioned due to complications during the construction process. Some of the remaining gauges provided reliable data, while others failed. The priority was identifying which gauges functioned properly and delivering accurate data.

These issues were addressed, and the actual strain at each level was filtered out from the raw strain data, using an extended filtering procedure involving low-pass, high-pass, and band-pass filtering for specific frequency ranges. Noise in the time history data usually originates from random, high-frequency disturbances due to environmental vibrations, electrical interference related to sensor limitations, or transmission errors that introduce rapid fluctuations into the signal. Drift occurs because of slow variations with time, which often arise from temperature variations, sensor instability, or long-term environmental effects, including the settlement of a structure and thermal expansion. Both noise and drift distort the accurate signal; hence, their filtering is indispensable for obtaining meaningful data.

As noted by Wood, L.C. 1968 [23], once dominant frequencies are identified, filters—such as low-pass, high-pass, or band-pass—can be applied to remove unwanted frequency components without compromising the structural integrity of the analysis. By carefully selecting cutoff frequencies, the filtered data can accurately reflect the structural response, free from distortion caused by external noise or irrelevant signals.

In this study, band-pass filters were employed, with cutoff frequencies tailored individually for each strain gauge through iterative testing to enhance data quality. While filtering significantly improved the clarity and reliability of the strain signals, some gauges remained inconsistent or unreliable. This suggests additional factors may have influenced data quality, including sensor calibration errors, installation defects, or localized noise sources.

The initial cutoff frequencies were chosen based on the structure's natural frequencies and then refined through a trial-and-error process to achieve the most accurate and realistic strain measurements.

#### 4.2.2 Foundation Strain Gauge Analysis

Based on the filtering process, some strain gauge data were deemed unusable due to issues with specific sensors. Gauges identified as reliable are shown in green, while unreliable ones are marked in red. The reliable gauges yielded accurate and consistent data, which is essential for effective long-term monitoring. In contrast, gauges that did not reflect the expected load-strain relationship were largely considered unreliable.

The testing setup relied on a generator due to the absence of utility power, which may have introduced additional noise and signal drift. Construction-related factors also contributed to data loss. Several gauges were damaged or lost during concrete placement, and among those that remained intact, additional failures occurred due to environmental exposure or electrical malfunctions. Despite these challenges, the data from the functioning gauges proved valuable. Figure 4-10 illustrates the distribution of reliable (green) and failed (red) strain gauges across each level of the structure.

To distinguish between reliable and unreliable gauges, the filtering process was essential. For example, Figure 4-11 presents the filtered strain results for the first, third, and fourth levels of the vertical inside gauges under torsional downstream loading for S-13-570. The strain values show a gradual decrease from the first to the fourth level, aligning with theoretical expectations that strain diminishes with depth.

Table 4-8 summarizes the sensor information depicted in Figure 4-10, identifying which gauges were deemed reliable based on their performance across all pull tests. Gauges that failed to produce consistent or accurate data during these tests were classified as unreliable.

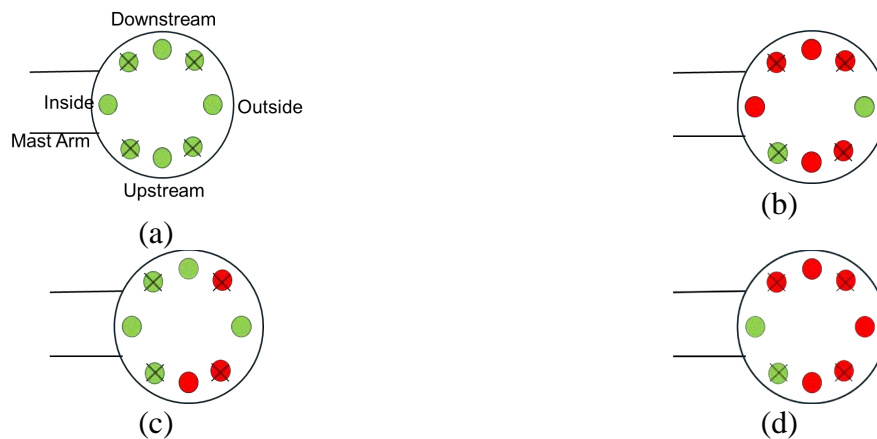


**Figure 4-10. Reliable and unreliable foundation strain gauges: (a) level 1, (b) level 2, (c) level 3, and (d) level 4**

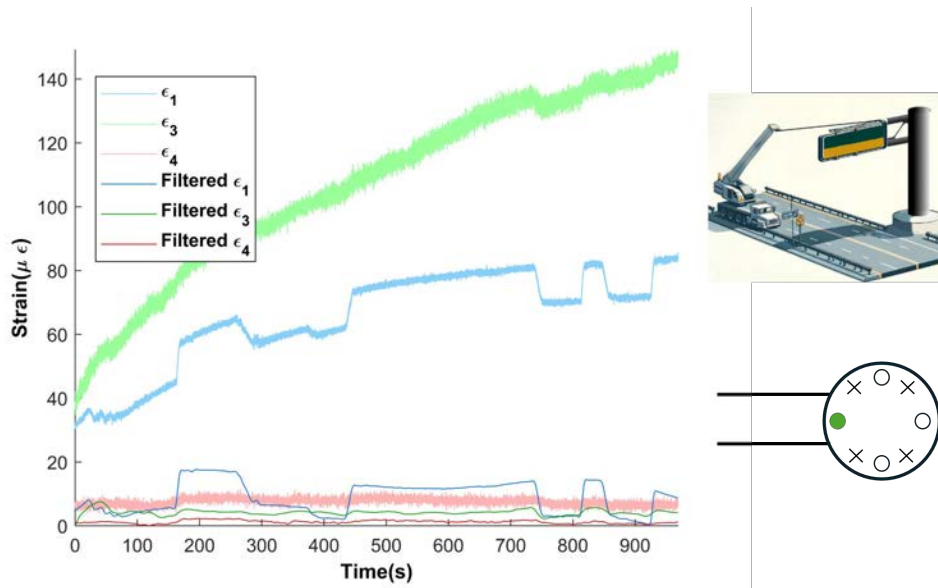


**Figure 4-11. Vertical inside strain data before and after filtering in torsional load case, S-13-570**

### 4.3 SAP2000 Model

A SAP2000 model was used for numerical analysis. Three-dimensional frame elements were used. The models for S-13-562, and S-13-570 are shown in Figure 4-12 and Figure 4-13, respectively. To validate the SAP2000 models, gauge data were analyzed and compared with the results for bending moments in the  $x$  and  $y$  directions as well as torsion at the base. Comparisons between the SAP2000 model results, including moments and torsion at the base, and the gauge data during torsional upstream testing for S-13-570 and S-13-562, are mentioned in the Appendix. The SAP2000 model demonstrates strong alignment with the gauge data, indicating that both models closely align with the measured data and the behavior of the real structures.

**Table 4-8: Table summarizing sensor info shown in Figure 4-10**

Structure ID	Level of Sensor	Sensor Position	Sensor Type	Sensor Reliable (Y/N)
S-13-570	1	VD <sup>25</sup>	VSG <sup>26</sup>	Y
S-13-570	1	VU <sup>27</sup>	VSG	Y
S-13-570	1	VI <sup>28</sup>	VSG	Y
S-13-570	1	VO <sup>29</sup>	VSG	Y
S-13-570	1	DDI <sup>30</sup>	DSG <sup>31</sup>	Y

<sup>25</sup> Vertical Downstream

<sup>26</sup> Vertical Strain Gauge

<sup>27</sup> Vertical Upstream

<sup>28</sup> Vertical Inside

<sup>29</sup> Vertical Outside

<sup>30</sup> Diagonal Downstream Inside

<sup>31</sup> Diagonal Strain Gauge

S-13-570	1	DDO <sup>32</sup>	DSG	Y
S-13-570	1	DUI <sup>33</sup>	DSG	Y
S-13-570	1	DUO <sup>34</sup>	DSG	Y
S-13-570	2	VD	VSG	N
S-13-570	2	VU	VSG	N
S-13-570	2	VI	VSG	N
S-13-570	2	VO	VSG	Y
S-13-570	2	DDI	DSG	N
S-13-570	2	DDO	DSG	N
S-13-570	2	DUI	DSG	Y
S-13-570	2	DUO	DSG	N
S-13-570	3	VD	VSG	Y
S-13-570	3	VU	VSG	N
S-13-570	3	VI	VSG	Y
S-13-570	3	VO	VSG	Y
S-13-570	3	DDI	DSG	Y
S-13-570	3	DDO	DSG	N
S-13-570	3	DUI	DSG	Y
S-13-570	3	DUO	DSG	N
S-13-570	4	VD	VSG	N
S-13-570	4	VU	VSG	N
S-13-570	4	VI	VSG	Y
S-13-570	4	VO	VSG	N
S-13-570	4	DDI	DSG	N
S-13-570	4	DDO	DSG	N
S-13-570	4	DUI	DSG	Y
S-13-570	4	DUO	DSG	N

**Table 4-9. Materials in SAP2000 software**

Type	Name	Properties
1	A500 Grade C Round	$F_y^{35} = 42 \text{ ksi}$
2	A709 Grade 36	$F_y = 36 \text{ ksi}$
3	A992	$F_y = 50 \text{ ksi}$
4	Foundation Concrete	$f'_c^{36} = 7 \text{ ksi}$
5	Steel Modulus of Elasticity	$E_s = 29,000 \text{ ksi}$
6	Concrete Modulus of Elasticity	$E_c = 150,807 \text{ ksi}$

<sup>32</sup> Diagonal Downstream Outside

<sup>33</sup> Diagonal Upstream Inside

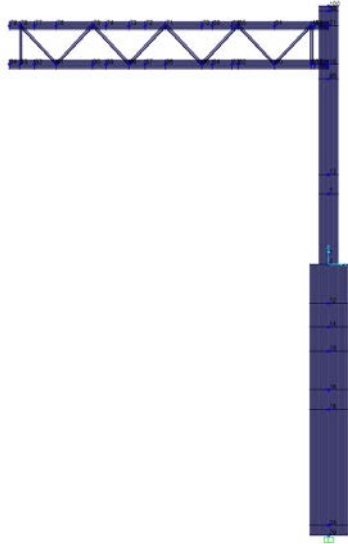
<sup>34</sup> Diagonal Upstream Outside

<sup>35</sup> Yield Strength

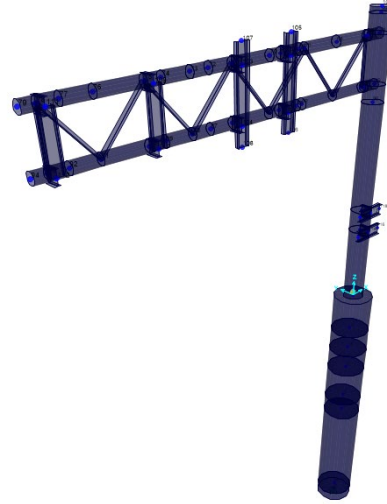
<sup>36</sup> Concrete Compressive Strength

**Table 4-10. Sections in SAP2000 software**

Type	Label	Shape	Material
1	Chord	PIPE10"SCH40	A500 Grade C Round
2	Bracing	L3×3×4	A709 Grade 36
3	Column	PIPE24"SCH40	A500 Grade C Round
4	VAM	W6×9	A992

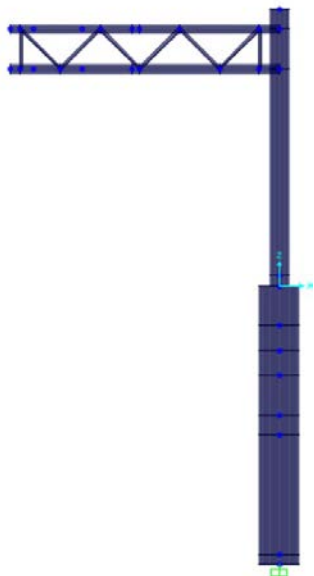


(a)

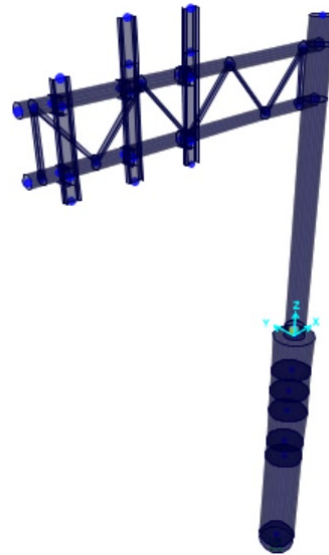


(b)

**Figure 4-12. SAP2000 model for S-13-562: (a) two-dimensional view and (b) three-dimensional view**



(a)



(b)

**Figure 4-13. SAP2000 model for S-13-570: (a) two-dimensional view and (b) three-dimensional view**

### 4.3.1 Modal Analysis

In SAP2000, modal analysis is an analysis that finds the natural frequencies, mode shapes, and dynamic characteristics of a structure. It helps identify how a structure will respond to dynamic loads due to wind, earthquakes, or vibrations by analyzing the behavior of the structure at each different natural mode.

The results of modal analysis in SAP2000 for S-13-562, and S-13-570 are shown in Table 4-11 and Table 4-12, respectively. The mode shapes corresponding to the first three modes are illustrated in the Appendix.

**Table 4-11. Natural frequencies based on SAP2000 Model for S-13-562**

Number of Modes	Period(sec)	Frequency (Cyc/sec)
1	0.606	1.650
2	0.384	2.601
3	0.168	5.946

**Table 4-12. Natural frequencies based on the SAP2000 Model for S-13-570**

Number of Modes	Period (sec)	Frequency (cycles/sec)
1	0.494	2.022
2	0.363	2.752
3	0.177	5.635

## 4.4 Free-Vibration Test

A free-vibration test evaluates a structure's dynamic response following an initial disturbance, without any continued external force. This test is used to determine key dynamic properties, including natural frequencies, damping ratios, and mode shapes. Understanding these characteristics helps engineers assess how the structure will perform under dynamic conditions such as wind or seismic activity. Free-vibration testing also plays a critical role in validating computational models—such as those developed in SAP2000—by ensuring they accurately predict the structure's dynamic behavior. This validation is essential for designing safer and more efficient structures.

Accelerometers were installed at the tip of the mast arm to measure accelerations in three directions: out-of-plane, vertical, and horizontal. The acceleration time histories recorded during the pluck test were used to determine the natural frequencies and damping ratio of the structure, which was crucial for understanding its dynamic behavior. Figure 4-14 illustrates the three accelerometers on both structures.

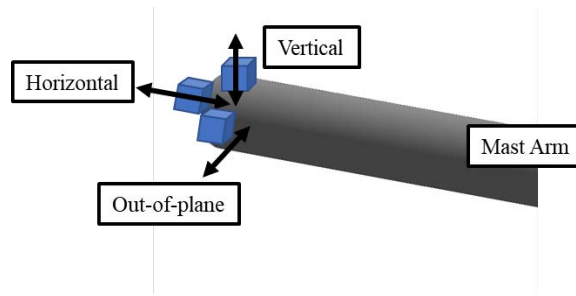


**Figure 4-14. Accelerometers in three directions on both structures**

#### 4.4.1 Acceleration Time History Analysis

The Power Spectral Density (PSD) function of acceleration time histories gives, in detail, how the energy of a signal is distributed across various frequency components. It thus becomes a significant tool for dynamic analysis in its ability to determine the response of a structure to time-varying loads. In this respect, by evaluating PSD, the structure's natural frequencies corresponding to significant peaks in the PSD curve can be identified. These natural frequencies provide the points that are most vulnerable when a structure undergoes resonance. The PSD also reflects the overall dynamic response of a structure because it shows how different frequency components of an input, for example, seismic activity or machinery-induced vibrations. Besides this, PSD analysis has also been used to validate computational models, like those developed in SAP2000, by comparing measured acceleration responses against simulated results. This comparison ensures that the model is accurate and enhances the confidence in the predictions [24].

Time histories of acceleration and PSD plots of acceleration are presented in the Appendix. From the PSD plots, the determination of modal response in different directions was made. The natural frequencies of the structure according to the PSD plots are presented in Table 4-13.

**Table 4-13: Summarizing natural frequencies for both structures and all 3 modes in free-vibration test for all acceleration directions**

Structure ID	Accelerometer	Natural Frequency (Hz) Mode 1	Natural Frequency (Hz) Mode 2	Natural Frequency (Hz) Mode 3
<b>S-13-570</b>	Out-of-plane	5.6	6.82	7.5
	Horizontal	2.03	2.37	3.29
	Vertical	2.37	4.8	7.15
<b>S-13-562</b>	Out-of-plane	2.6	6.82	7.5
	Horizontal	1.65	2.18	4.12
	Vertical	2.2	4.37	6.58

The logarithmic decrement method is one of the most common techniques for obtaining a system's damping ratio from its acceleration time history. It uses measurement of the decay of oscillations in a free-vibration response.

To apply this method, peak amplitudes  $A_n$  and  $A_{n+k}$  are first identified from the acceleration time history in free vibration test. The logarithmic decrement  $\delta$  is calculated as the natural logarithm of the ratio of two peak amplitudes, as shown in equation (4-31).

$$\delta = \frac{1}{k} \ln\left(\frac{A_n}{A_{n+k}}\right) \quad (4-31)$$

where  $k$  is the number of cycles or periods between the selected peaks.

Once  $\delta$  is calculated, the damping ratio  $\zeta$  can be determined by equation (4-32).

$$\zeta = \frac{\delta}{\sqrt{4\pi^2 + \delta^2}} \quad (4-32)$$

Based on the calculations for both structures, the damping ratio was determined to be 0.56% for S-13-570 and 0.44% for S-13-562.

#### 4.5 Summary of Static and Free Vibration Tests

This chapter presented a complete analysis of the torsional and moment transfer from static load tests in two test structures. For calculating torsion and moments rosette strain gauges that installed on the pole were utilized, and the results compared against loadcell data. The comparison demonstrated a high level of agreement, confirming the reliability of gauges.

To evaluate the rotational and translational responses of the structures, string potentiometer data were analyzed. The results indicated that increased torsional loading resulted in greater rotational deformation. The maximum calculated rotation was 0.002, and 0.01 degrees for S-13-562 and S-13-562, respectively. Additionally, maximum translational displacement occurred in the y-direction, consistent with the direction of the applied load.

Then, free-vibration tests were conducted to validate the dynamic response and show a good alignment with natural frequencies and mode shapes of FEM.

The major goal of the static and free vibration tests was to assure that the SAP2000 models for both structures are accurate. Therefore, after validation of strain gauges, numerical structural results compared to the experimental results. This comparison shows close alignment and concludes that the models can calculate structural responses under different load conditions accurately. This validation helps to understand how the structure will respond in various weather and load conditions, such as wind and traffic during long-term monitoring.

## 5. LONG-TERM MONITORING

### 5.1 Structural Health Monitoring Data Collection

Real-time data acquisition of all installed instruments began in December 2023 for both structures. Without a predefined trigger point for capturing critical data, real-time acquisition led to data being overwritten, making it impossible to maintain a continuous record of structural responses over time. To address this, an appropriate trigger threshold of  $\pm 0.15g$  was established. This threshold was determined through a statistical analysis of an accelerometer dataset, ensuring that significant structural events were captured without unnecessary data loss.

The statistical thresholding technique given in equation (5-1) was used to find an optimum trigger point based on data recorded before April 2024, where  $\mu$ ,  $\sigma$ ,  $x$ , and  $Z$  indicate mean, standard deviation, data, and Z-score, respectively.

$$Z = \frac{x - \mu}{\sigma} \quad (5-1)$$

When acceleration values exceeded the predefined trigger threshold, data recording was automatically initiated across all instruments. The recorded dataset includes measurements from rosette strain gauges, used to assess torsional and bending moments at the base, as well as accelerometer data for evaluating the structure's dynamic response, including natural frequencies. Although the instrumentation setup closely resembles that used during the pull tests, the long-term monitoring dataset does not include string potentiometer readings. Instead, it incorporates data from an anemometer, capturing wind speed and direction—factors not recorded during the pull tests. A summary of the recorded data is presented in , and the data distribution over one week (the first week of April 2024) is illustrated in .

**Table 5-1: Overview of data acquisition**

Month	Weeks
December 2023	2
January 2024	3
February 2024	3
March 2024	4
April 2024	5
May 2024	4
June 2024	4
July 2024	4
August 2024	4
September 2024	4
October 2024	4
November 2024	4
December 2024	4
January 2025	4

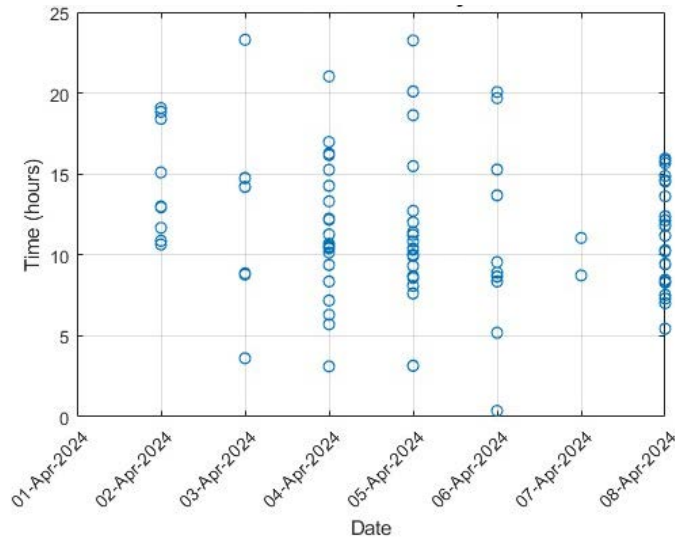


**Figure 5-1: Distribution of data acquisition of the first week of April**

### 5.1.1 Wind Data

The wind data needed preprocessing because the anemometer was mounted in a direction other than global north. As illustrated in Figure 5-2, the anemometer was installed in alignment with the mast arm. According to the anemometer’s manual, it recorded  $0^\circ$  when the wind flows parallel to the mast arm, specifically from the pole toward the mast arm. However, in the standard coordinate system, north is oriented at an angle of  $45^\circ$  relative to the mast arm, positioned between the inside and upstream sides. Consequently, to ensure consistency in data interpretation, wind direction measurements were adjusted to reflect this angular difference between the anemometer’s reference frame and the standard north alignment. In the usual coordinate system adopted for wind rose plots, the anemometer’s  $0^\circ$  corresponds to  $225^\circ$ .

The wind direction measurements were converted to reference the standard north to use in wind rose diagrams. In addition, the mast arms were assumed to be oriented in the northeast direction. Figure 5-3 shows the anemometer installation and provides a reference from the manual for determining the  $0^\circ$  orientation of the anemometer.

Throughout the year, the dominant wind direction shifted between west-northwest (WNW) and northwest (NW). In April, the strongest winds originated from WNW, a pattern that continued through May and June with slight variations. During July, August, and September, the wind weakened and shifted slightly towards the south and the northwest (NW). As the year progressed into October and November, the wind gradually returned to WNW, gaining strength. By December and January, the pattern remained like April, with winds predominantly from WNW, though at slightly lower speeds. To enhance the interpretation of these patterns, wind rose diagrams were utilized, providing a comprehensive visualization of the frequency and intensity of wind flow from different directions. A wind rose diagram is a graphical representation of wind speed and direction over a specified period. It provides insights into the dominant wind direction, the frequency of occurrence, and variations in wind speed. The wind directions are indicated by the compass labels around the diagram (N, NE, E, etc.), showing the directions from which the wind originates. The length of each bar represents the frequency of wind coming from that direction, and different

percentages are shown on the bars. The concentric circles represent the percentage of time the wind blows from a specific direction. The outermost circles indicate a higher frequency, while the innermost circles represent a lower frequency. The color-coded segments indicate different wind speed ranges. The legend categorizes the wind speeds in miles per hour (mph), with different colors representing different intensity levels.

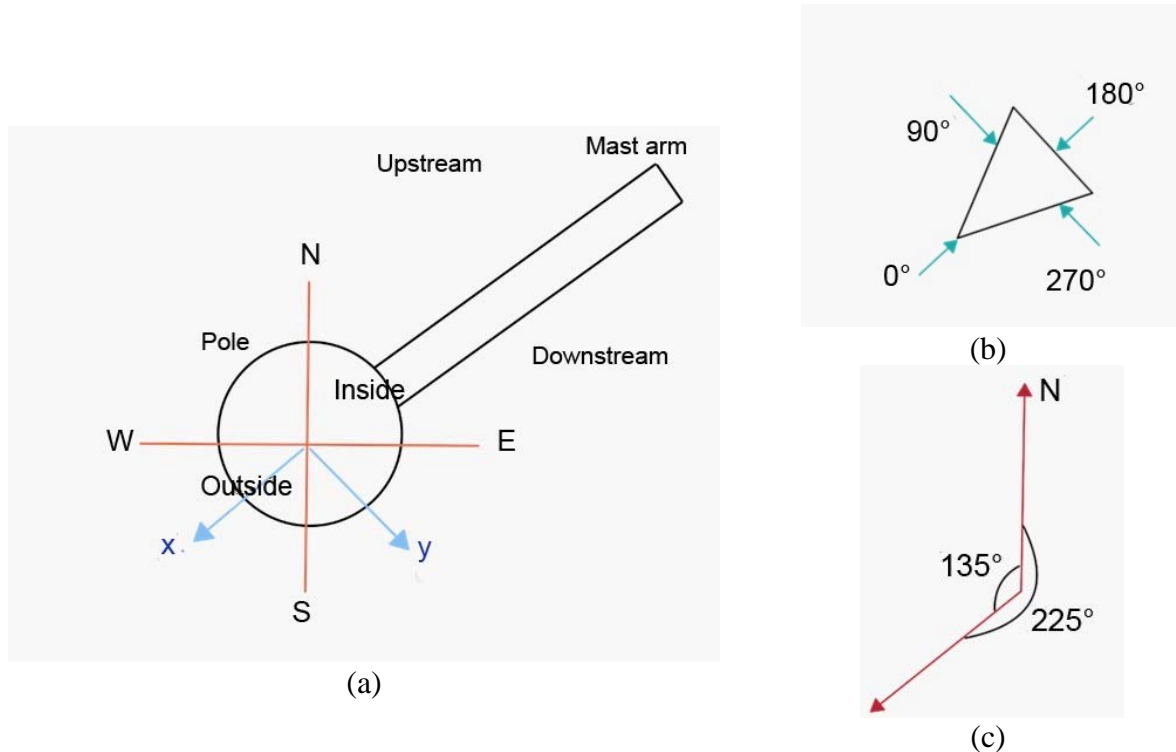


**Figure 5-2. Anemometer placement and orientation: (a) standard coordinate system with structural reference, (b) wind direction measurement using anemometer, and (c) alignment of the anemometer's 0° reference with standard north**

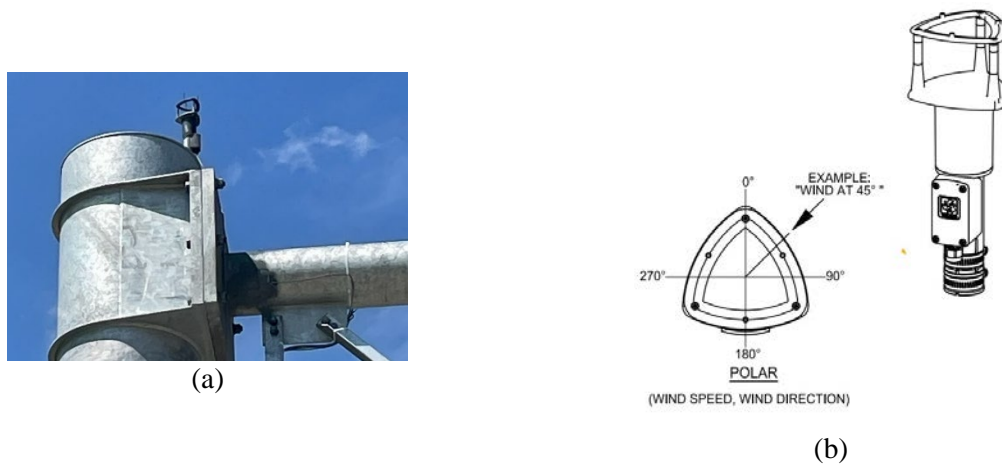


**Figure 5-3. Anemometer installation and reference: (a) anemometer mounted on top of the structure and (b) anemometer manual illustrating wind direction measurement and polar coordinate system**

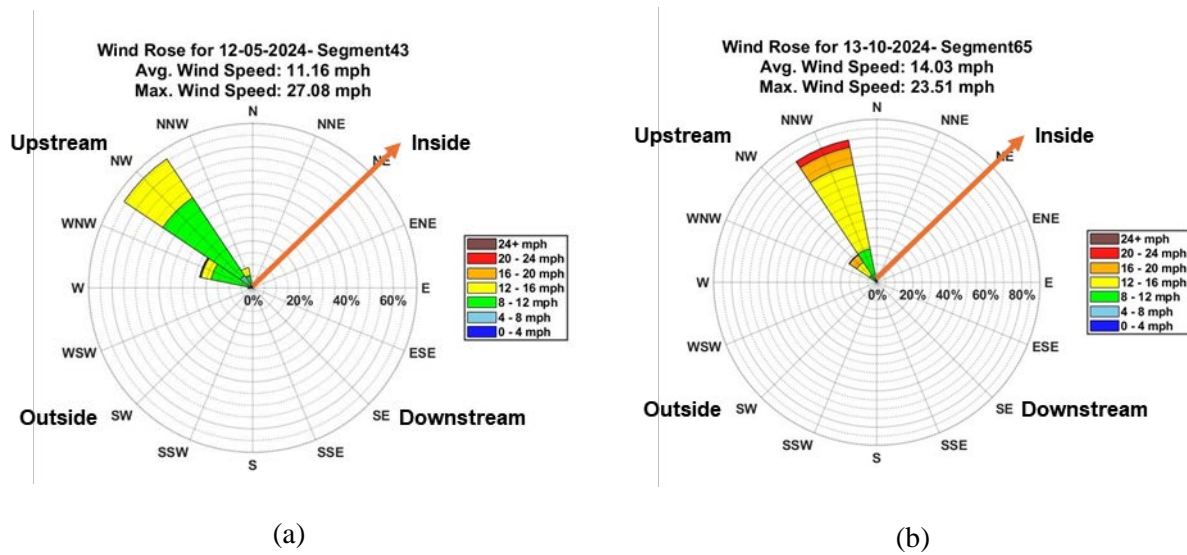


**Figure 5-4: (a) Highest wind event for S-13-562 and (b) highest wind event for S-13-570**

For example, the highest wind events for structures are shown in Figure 5-4. The arrow indicates the mast arm of the structure, and “inside,” “outside,” “upstream,” and “downstream” indicate the pole sides. The wind rose diagrams during the long-term monitoring for both structures are shown in the Appendix.

## 5.2 Acceleration Time History Analysis

To analyze the dynamic response of the structure, the acceleration time histories and their PSD functions in each direction were computed. The process of obtaining natural frequencies is the same as free vibration tests. The natural frequencies for the vertical, horizontal, and out-of-plane directions are presented in Table 5-2. A comparison between Table 4-13 and Table 5-2, indicates the alignment of the structural response in the dynamic analysis between the free-vibration test and the long-term analysis based on the accelerometer data. Acceleration time histories and the corresponding PSD plots are shown in the Appendix.

## 5.3 Data Analysis

Due to the nature of the data acquisition process, distinct segments within each month indicate periods when data were collected continuously. These segments correspond to instances where the structural acceleration exceeded the trigger point, marking significant wind-induced responses. However, the data were not recorded continuously throughout each week, necessitating dataset segmentation to identify the most extreme wind event over the entire data acquisition period.

For all wind data analyses, a three-second gust averaging method was applied. This approach was essential because wind speed fluctuations occur over very short time intervals, and averaging over a three-second period provides a more representative measure of the wind loads impacting the structure. Instead of capturing instantaneous wind gusts, which can be highly

variable, the three-second averaging smooths out rapid fluctuations, providing a better estimate of the wind load influencing structural response.

**Table 5-2: Summarizing natural frequencies for both structures and all 3 modes for different acceleration directions**

Structure ID	Accelerometer	Natural Frequency (Hz) Mode 1	Natural Frequency (Hz) Mode 2	Natural Frequency (Hz) Mode 3
S-13-570	Out-of-plane	2.59	-	-
	Horizontal	2.10	2.9	3.32
	Vertical	2.56	8.8	-
S-13-562	Out-of-plane	2.59	6.5	7.21
	Horizontal	1.67	3	4.22
	Vertical	3	4.8	5.2

To calculate this, wind speed data were first collected at high-frequency intervals, every 0.033 seconds, using an anemometer. The averaging process involved applying a moving average over each three-second window (90 data points), where the wind speeds recorded during that time frame were summed and divided by the number of data points within the event. The three-second gust speed at time  $t$  is expressed in equation (5-2).

$$V(t) = \frac{1}{N} \sum_{i=t}^{t+N-1} V_i \quad (5-2)$$

where  $V(t)$  is the three-second averaged wind speed,  $N$  is the number of samples in three seconds ( $N$  is 90), and  $V_i$  is the wind speed at each recorded time step. This moving average is computed throughout the dataset.

Using wind data obtained from an anemometer, the wind direction and wind speed in each segment were utilized to compute the perpendicular and the tangential wind components on the structure. These components were calculated using equations (5-3) and (5-4).

$$V_{\perp} = V_g \cdot \sin(\theta) \quad (5-3)$$

$$V_{\parallel} = -V_g \cdot \cos(\theta) \quad (5-4)$$

Where  $V_{\perp}$  is the perpendicular wind vector,  $V_{\parallel}$  is the tangential wind vector,  $V_g$  is the gust wind speed measured by the anemometer after 3-second gust averaging, and  $\theta$  is the wind direction recorded. The negative sign in equation (5-4) to calculate tangential wind speed is used to align the wind vector with the positive  $x$  direction.

The computation of torsion and moments follows the same methodology as the static load tests, utilizing the installed rosette strain gauges.

In long-term monitoring, an additional challenge arises due to drift in strain gauge readings over extended periods, which can be attributed to several factors. Thermal effects cause expansion and contraction, leading to gradual drifts in recorded strain values. Additionally, environmental

changes like humidity or the warmth of the sun may impact sensor performance over time. To maintain accuracy, rosette strain gauge readings must be filtered to eliminate drift effects not due to wind. The filtering process follows the same methodology outlined in the static test procedures for the foundation gauges, ensuring that only relevant structural response data are retained.

### 5.3.1 High Wind Analysis

The highest wind events for both structures resulted in the most significant structural responses, which are critical to understand because they can be classified as extreme wind events. To verify the accuracy of these data and ensure that they provide reliable results, the transferred torsion and moments were also calculated using the validated FEM.

To properly integrate the wind time series into the model, it is important to note that the perpendicular and tangential wind vectors, were used to calculate wind pressures and forces. The wind data were applied by considering the structural element’s characterizations and utilizing equation (5-5) according to chapter three of the LRFD SLTS [16] to ensure accurate representation of wind effects.

$$P_z = 0.00256K_zK_dGV^2C_d \quad (5-5)$$

where  $V$  is the wind speed in mph;  $K_z$  is the height and exposure factor, which is one for all elements;  $K_d$  is the directionality factor, which depends on the element (shown in Table 5-3);  $G$  is the gust effect factor, which is taken to be 1.14; and  $C_d$  is the drag coefficient, which depends on the element characteristics. Note that the wind speed in each time step can be different.

To accurately apply wind forces to the structure, four categories of elements were considered:

1. Signs: In S-13-562, the sign was connected to eight points on the mast arm, whereas in S-13-570 it was connected to six points due to the presence of two separate signs. The wind force acting on the signs was applied to these respective nodes on the mast arm, with a unit of kips.
2. Mast arm: The wind pressure, measured in kips per foot (kips/ft), was applied to the mast arm sections directly exposed to wind, excluding the areas covered by signs.
3. Pole: The wind pressure was applied as a distributed load along the length of the pole, with units of kips/ft, to account for its exposure to wind forces.
4. Truss: Similar to the mast arm, the wind pressure was applied as a distributed load (kips/ft) to the truss sections that were not covered by signs, ensuring accurate force distribution in the structural analysis.

**Table 5-3. Wind coefficients for elements**

Element	Directionality Factors ( $K_d$ )	Wind Drag Coefficients ( $C_d$ )
Sign	1	1.134
Mast Arm	0.85	1.1
Pole (Round Section)	0.95	1.1
Truss	0.95 (conservative)	1.7

### 5.3.2 Structural Response under High Wind for S-13-570

The analyzed structural response of S-13-570 under highest wind event that is mentioned in Figure 5-4 (b) is shown as an example. The base reaction for S-13-562 under highest wind speed is mentioned in the Appendix. Figure 5-5 presents the base reaction to the presented wind load. The bending moment ( $M_x$ ) at the base is demonstrated in Figure 5-5 (a) with the orange curve indicating  $M_x$  values using rosette strain gauges and the blue curve indicating results from the SAP2000 model. There is a need to account for potential drift of strain gauge measurements when carrying out long-term monitoring. The comparison of torsion is indicated in Figure 5-5 (b).

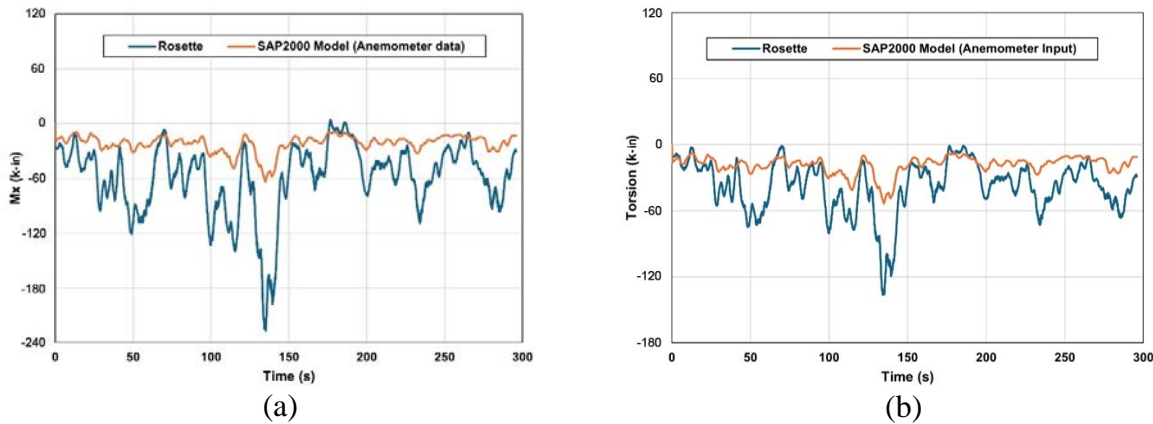


**Figure 5-5. Base reaction in S-13-570 for the highest wind: (a)  $M_x$  and (b) torsion**

As it shown before in Figure 5-4, the highest wind event measured by anemometer during the long-term monitoring was significantly lower than the standard design wind speed of these structures which is 115 mph. To evaluate structural response under the extreme wind events, a stochastic wind model was developed.

Results from the finite element analysis with different stochastic wind loads are presented in Table 5-4. The analysis indicates the peak shear force for S-13-562 is 5.2 kips and the peak bending moment is 1,440 k-in, which is necessary input parameters for L-Pile analysis. The results for S-13-570 show the maximum shear is 5.2 kips and the maximum bending moment is 1,752 k-in. S-13-570 shows higher structural base reactions in all three measured responses compared to S-13-562 across all wind speed levels.

**Table 5-4. Base reaction of different of stochastic wind model**

Maximum Wind Speed (mph)	Average Wind Speed (mph)	S-13-562			S-13-570		
		Torsion (k-in)	$M_x^{37}$ (k-in)	Shear (k)	Torsion (k-in)	$M_x$ (k-in)	Shear (k)
43	30	120	144	0.55	180	216	0.78
60	50	300	360	1.3	360	420	1.5
82	70	540	600	2.1	696	816	2.6
98	90	840	960	3.5	960	1,140	4
121	110	1,200	1,440	5.2	1,440	1,752	6.3

<sup>37</sup> Bending moment in  $x$  direction

## 5.4 Checking Alternative Foundation Designs

To understand the maximum bending moment in the foundation for highest wind, the structural base responses for highest wind (Table 5-4) considered as input for the L-Pile analysis. This analysis for S-13-562 foundation is obtained based on the soil layer data provided in the geotechnical report and the layers mentioned in Chapter 3, and it is shown in Figure 5-6 (a). Inputs to L-Pile analysis based on the applied load are as follows:

- Shear force: 5,200 lb (Condition 1)
- Moment: 1,440,000 in-lb (Condition 2)
- Axial load: 6,200 lbs (structure weight)

The bending moment increases at depth, to a peak at 1,500 in-kips at a depth of 5 ft. The maximum moment is generally at the location where soil resistance is also maximum. The load inputs for L-Pile analysis for S-13-570 are as follows:

- Shear force: 6,300 lb (Condition 1)
- Moment: 1,752,000 in-lb (Condition 2)
- Axial load: 5,600 lbs (structure weight)

The results of L-Pile analysis are shown in Figure 5-6 (b). The bending moment rises with depth and reaches a peak of around 2,100 k-in at a depth of around 5 ft (not considering the first layer of the soil), and then it decreases.

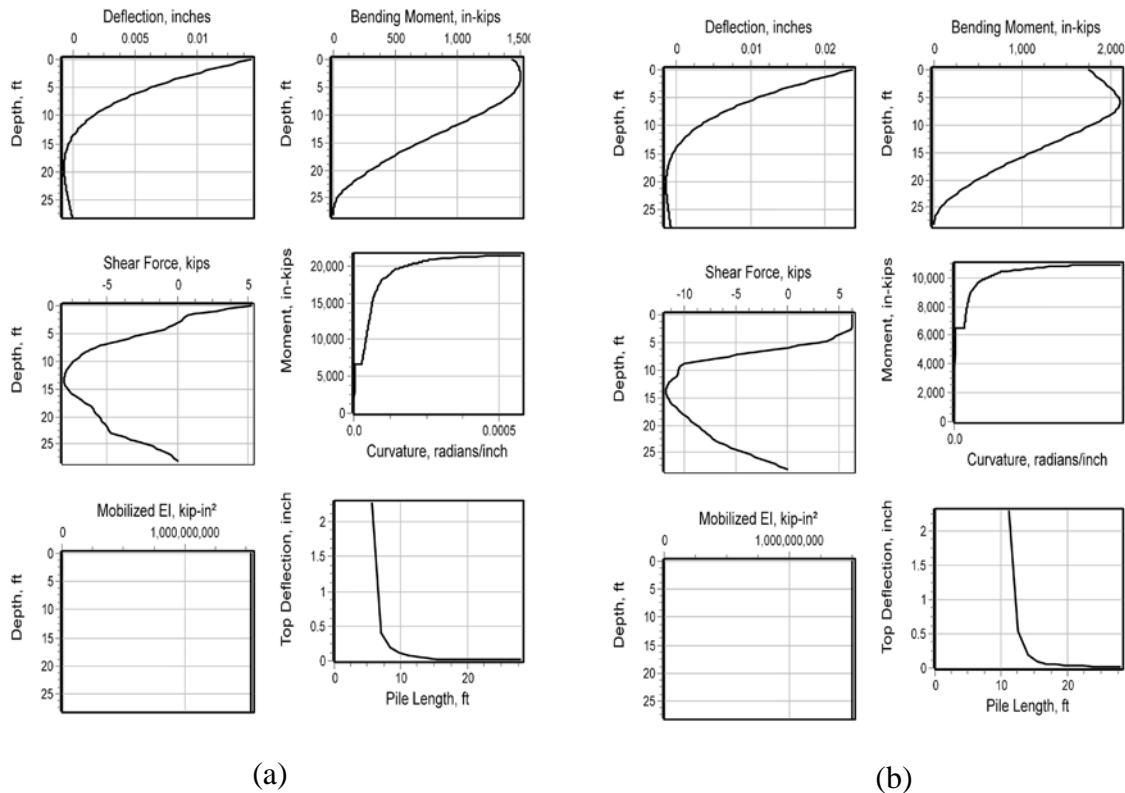


Figure 5-6: L-Pile analysis for highest stochastic wind: (a) S-13-562, and (b) S-13-570

Two foundations MCIV/TFIV and TFII considered as examples of standard foundation based on the WisDOT Bridge Manual [1]. Table 5-5 refers to foundation characteristics of MCIV/TFIV and Table 5-6 refers to foundation characteristics of TFII.

**Table 5-5. Foundation characteristics of MCIV/TFIV**

<b>Foundation Properties</b>	<b>Level 1</b>
Moment of Inertia(in. <sup>4</sup> )	104,007
Torsional constant(in. <sup>4</sup> )	208,014
Shear area(in. <sup>2</sup> )	1,028
Section modulus(in. <sup>3</sup> )	5,452
Plastic modulus(in. <sup>3</sup> )	9,255
$M_{crack}$ (k-in.)	4,395
Radius of Gyration	9.5

**Table 5-6. Foundation characteristics of TFI**

<b>Foundation Properties</b>	<b>Level 1</b>
Moment of Inertia(in. <sup>4</sup> )	61,393
Torsional constant(in. <sup>4</sup> )	122,787
Shear area(in. <sup>2</sup> )	790
Section modulus(in. <sup>3</sup> )	3,671
Plastic modulus(in. <sup>3</sup> )	6,233
$M_{crack}$ (k-in.)	3,026
Radius of Gyration	8.3

### **5.5 Parametric Study Results for Foundation Optimization**

To optimize the foundation design, a linear parametric analysis was used. The analysis examined the rotational and translational behavior of drilled shaft foundations under applied torque and bending moments. To achieve this, a range of foundation radius between 24 to 48 in. and a range of foundation length from 12 to 28 ft. considered. Although the loading conditions used in the parametric analysis (considering 2,520 k-in for torque and 5,184 k-in for bending moment) were higher than those observed in the highest stochastic wind model, linear scaling of the results is possible because it is a linear parametric analysis. The highest structural response, 1,440 k-in for torque and 1,752 k-in for bending moment, are approximately one-third of the loads applied in the parametric study. Therefore, the resulting displacements reported in the parametric models can be proportionally reduced to show foundation response under the highest wind.

The FEM set up for nonlinear analysis. The concrete shaft is modeled as a cylinder, with a portion above the ground surface, and the bottom of the shaft considered above the base of the soil domain. The soil domain radius is defined as three times the shaft diameter, and an outer layer is included to model an infinite boundary. The resulting stress distribution confirms that these dimensions are sufficient to avoid boundary effects.

Table 5-7 shows the geometric parameters and soil properties shown in Table 5-8. Loads that are considered at the top of the shaft are mentioned in Table 5-9. The parametric study was conducted for 25 models and the Figure 5-7 (a) shows the relationship between foundation shaft radius and top rotation under the applied torque. Figure 5-7 (b) shows the top rotation based on the shaft depth. The soil translation based on changes in radius and shaft depth under the applied bending moment is shown in Figure 5-8.

**Table 5-7: Geometric parameters**

<b>Geometric Parameters</b>	<b>Value</b>
$R_{\text{soil}}^{38}$	72 in.
$H_{\text{soil}}^{39}$	168 in.
$R_{\text{concrete}}^{40}$	24 in.
$H_{\text{concrete}}^{41}$	144 in.
$R_{\text{infinite}}^{42}$	84 in.
$L_{\text{shaft}}^{43}$	24 in.
$H_{\text{base}}^{44}$	24 in.
<b>Soil Domain Radius Factor</b>	3
<b>Radius Extended</b>	12 in

**Table 5-8: Soil parameters**

<b>Soil (sand) Properties</b>	<b>Value</b>
$E_s^{45}$	2900 psi
<b>Cohesion</b>	1 psi
<b>Internal Angle of Friction</b>	24 degrees
<b>Hardening Modulus</b>	1 psi

**Table 5-9: Load at the top of the shaft**

<b>Load Case</b>	<b>Torque</b>	<b>Bending Moment</b>
<b>1</b>	2,520 k-in	0
<b>2</b>	0	5,184 k-in
<b>3</b>	2,520 k-in	5,184 k-in

Low cohesion of 1 psi is considered to maintain the convergence of parametric analysis. Under drained conditions, clean sand is usually considered to have little cohesiveness. But a low cohesion value can account for the unsaturated conditions, and the grain interlocking. This minor cohesion has negligible influence on the overall shear strength, which is primarily governed by internal friction angle.

---

<sup>38</sup> Soil radius

<sup>39</sup> Soil height

<sup>40</sup> Concrete radius

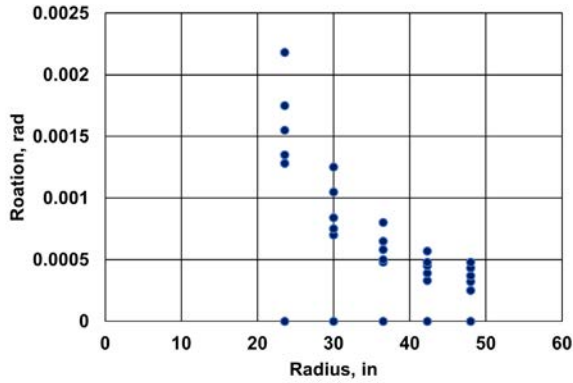
<sup>41</sup> Foundation depth

<sup>42</sup> Outer radius for infinite model

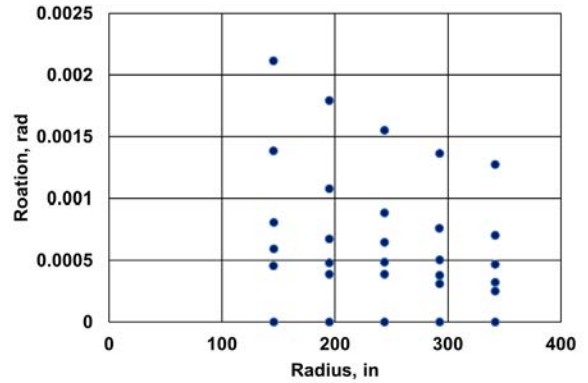
<sup>43</sup> Shaft above grade

<sup>44</sup> Distance from bottom of shaft to bottom of soil domain

<sup>45</sup> Modulus of Elasticity of soil

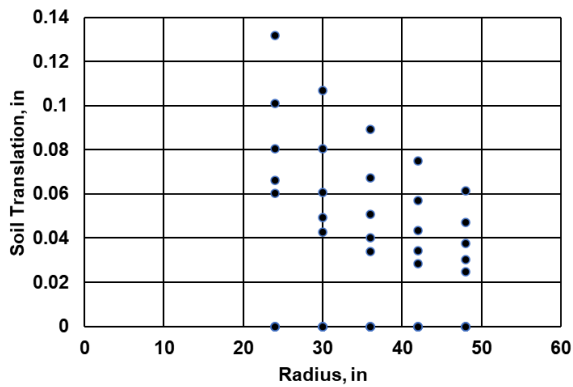


(a)

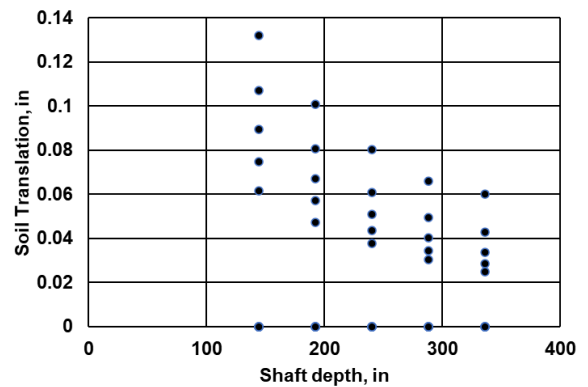


(b)

**Figure 5-7: Top rotations (a) rotation – radius, (b) rotation - shaft depth**



(a)



(b)

**Figure 5-8: Soil translation: (a) translation – radius, (b) translation – shaft depth**

According to the FEM response for different shaft models, the drilled shafts that had the lowest translation values were those with greater diameters ( $\geq 42$  in.) and intermediate depths ( $\geq 24$  ft.), as expected. This finding suggests that these foundations perform well for strong torsional and bending loads. In contrast, the result suggests that for less demanding loads (when structures are impacted by less wind and corresponding torque and moment), some intermediate drilled shaft designs (such as a 36-in. radius and a 20-ft. depth) can provide an effective, optimized design between performance and material consumption. Actual refinement of the current WisDOT standard sign structure foundations would require more detailed analysis that was not part of this project scope.

## 6. CONCLUSIONS

The research work presented in this study is significant in the sense that it provides an understanding of the structural response of traffic sign structures due to wind loads, specifically moment and torsion load transfer mechanisms.

Two traffic sign structures, S-13-562 and S-13-570, located in different soil conditions, were instrumented and subjected to pull tests involving statically increasing loads. These tests helped characterize the loads, stresses, and strains within the structures and their foundations. Since the structures remained in service, the applied loads engaged only 12–40% of the shafts' ultimate capacity, as estimated from L-pile analysis. While the tests primarily captured the shafts' linear response and were not sufficient to define their full capacity, they proved valuable for evaluating the performance of the installed strain gauges and provided a foundation for validating numerical models.

The long-term structural health monitoring continued for a year after instrumentation. Wind observed at the two sites were at a maximum speed of 27 mph which is 23% of the design wind speed of 115 mph. Apparently, the structure and foundation were only stressed to a fraction of ultimate design. However, this data was used to verify numerical models. Due to low winds observed at the location of structures, synthetic winds were generated and applied to the finite element model (FEM). These stochastic winds were used to assess the structural response and loads transferred to the shafts at higher wind speed ranges. The loads at the top of the shaft were transferred to the L-Pile to characterize the maximum bending moment in the foundation.

Traffic sign support structures were loaded with complex load combinations by wind loads, which impose large moments and torsional stresses on the foundation.

- For S-13-562, the maximum torsion was around 600 k-in., with a maximum bending moment of 1,600 k-in. in pull tests.
- Maximum measured torsion at the structure base was approximately 1,200 k-in. for S-13-570. The maximum bending moment in the  $x$ -direction at the base was 2,000 k-in., with the  $y$ -direction bending moment being less at around 200 k-in in the pull tests for S-13-570.

The lateral-torsional response difference confirms that bending moments control lateral loading conditions, and torsion is more influential in structural rotation. This helped to consider the moment for shaft rotation in parametric study and torque load case for calculating rotation at the top of the shaft.

Soil conditions strongly influenced torsional resistance in the drilled shaft. Soil parameters considered in the parametric modeling of drilled shafts play an important role in FEM to obtain the rotation and translation of the shaft under torque and moment. L-Pile and T-Pile analysis showed that soil stiffness varied with depth, affecting the bending moment and rotation along the shaft.

Long-term wind load and structural response monitoring provided critical information about the in-service performance of the traffic sign structures. Real-time sensors and data analysis helped to understand the effect of real wind and environmental conditions on the traffic sign structures.

Considering the acceleration time history, the damping ratio was determined to be 0.56% for S-13-570 and 0.44% for S-13-562.

To achieve an optimized foundation design, it is essential to consider structural limitations, loading conditions, and soil characteristics. A parametric study was conducted using linear analysis of 25 shaft models developed in finite element modeling (FEM). The results support the feasibility of reducing shaft length without compromising performance. The study further suggests that shorter shaft types—such as the Two-Chord Truss Full Type II (TFII) or Type IV (TFIV)—can offer a more efficient and balanced design in terms of structural performance and material usage when compared to the longer Two-Chord Cantilever Type IV (TCIV). However, this is only based on numerical analysis and require further experimental campaigns that load the pile shaft to the ultimate load and characterize the shaft behavior accordingly. Actual refinement of the current WisDOT standard sign structure foundations would require more detailed analysis that was not part of this project scope.

The serviceability limit of 1-in. top-of-shaft translation set by the WisDOT Bridge Manual to control the base movement is higher than the soil translation that was captured from parametric study. Therefore, if the foundation rotation and translation remain within acceptable performance bounds, a more refined limit, 0.5 in. (more conservative) to 0.2 in., could be adopted for optimization of the foundation size. In the FEM analysis, even with the full parametric loads, shaft models resulted in translation below 0.2 inches. Therefore, under the actual lower wind loads observed, shafts with smaller height can still satisfy even stricter serviceability limits.

Although the results of this research show valuable insight into the transferred torsional and bending moment of cantilevered sign structures under wind load, some constraints should be mentioned. First, there is a possible noise and drift in data acquisition system and sensor readings, especially over the long-term monitoring. Furthermore, although the finite element models were validated using experimental data, they are based on linear assumptions and do not completely reflect complicated wind dynamic characteristics. To further evaluate and generalize the results, future research should take into account larger geotechnical variability and possible foundation failure modes under higher loading conditions. This could be achieved by conducting tests on pile shafts that are not in service and could be engaged up to their ultimate limit state.

It should be noted that the design wind speeds in ASCE 7-16 (basis for WisDOT standardized designs) and consequently ASCE 7-22 are risk targeted speeds that are derived from probabilistic analysis and for traffic structures are normally based on return period of 700 years (assuming a risk category II). With Wisconsin being in a non-hurricane prone region, the likelihood of structure experiencing extreme wind speeds (e.g., >100 mph) is rare and longer-term monitoring is needed to capture meaningful data.

## 7. REFERENCES

- [1] Wisconsin Department of Transportation. LRFD Standardized Overhead Sign Structure Plans, WisDOT Bridge Manual. 2025.
- [2] Canning KT. Bridge Design Manual 2005.
- [3] Dexter RJ, Ricker MJ. Fatigue-Resistant Design of Cantilevered Signal, Sign, and Light Supports. Washington, D.C.: National Academies Press; 2002.
- [4] Paiva F, Barros RC. Integrity, reliability and failure of mechanical systems analysis of the stability and design of cantilevered sign supports in highways.
- [5] Constantinescu G, Bhatti A, Tokyay T. Final report TR-559 improved method for determining wind loads on highway sign and traffic-signal structures.
- [6] Zuo D, Smith DA, Mehta KC. Experimental study of wind loading of rectangular sign structures. *Journal of Wind Engineering and Industrial Aerodynamics* 2014;130:62–74. <https://doi.org/10.1016/j.jweia.2014.04.005>.
- [7] Tsai LW, Alipour A. Studying the wind-induced vibrations of a traffic signal structure through long term health monitoring. *Eng Struct* 2021;247. <https://doi.org/10.1016/j.engstruct.2021.112837>.
- [8] Jafari M, Sarkar PP, Alipour AA. A numerical simulation method in time domain to study wind-induced excitation of traffic signal structures and its mitigation. *Journal of Wind Engineering and Industrial Aerodynamics* 2019;193. <https://doi.org/10.1016/j.jweia.2019.103965>.
- [9] Yan G, Dyke SJ, Irfanoglu A. Experimental validation of a damage detection approach on a full-scale highway sign support truss. *Mech Syst Signal Process* 2012;28:195–211.
- [10] Aguilar Vidal VH. Torsional Resistance of Drilled Shaft Foundations. Auburn University, 2018.
- [11] Barbosa AR, Stuedlein AW, Li Q. Torsional Safety of Highway Traffic Signal and Signage Support. 2017.
- [12] South Carolina Department of Transportation (SCDOT). Chapter 16 Deep Foundations Geotechnical Design Manual. 2022.
- [13] Li Q, Stuedlein AW, Barbosa AR. Torsional load transfer of drilled shaft foundations. *Journal of Geotechnical and Geoenvironmental Engineering* 2017;143:04017036.
- [14] Sim C, Song CR, Kreiling B, Co- PE, Puckett J. High-mast tower foundation.
- [15] Sun Z, Krishnan S, Hackmann G, Yan G, Dyke SJ, Lu C, et al. Damage detection on a full-scale highway sign structure with a distributed wireless sensor network. *Smart Struct Syst* 2015;16:223–42. <https://doi.org/10.12989/sss.2015.16.1.223>.
- [16] AASHTO LRFD specifications for structural supports for highway signs, luminaries, and traffic signals. Aashto 2015.
- [17] Li Q, Stuedlein AW. Factors Affecting the Torsional Response of Deep Foundations. *Geotechnical Earthquake Engineering and Soil Dynamics V*, American Society of Civil Engineers Reston, VA; 2018, p. 368–78.

- [18] Thiyyakkandi S, McVay M, Lai P, Herrera R. Full-scale coupled torsion and lateral response of mast arm drilled shaft foundations. *Canadian Geotechnical Journal* 2016;53:1928–38.
- [19] Pinjan A, Zahui M. Monitoring of a traffic sign structural support vibrations. 24th international congress on sound and vibration, 2017.
- [20] American Association of State Highway and Transportation Officials. AASHTO LRFD Bridge Design Specifications. Washington, DC: n.d.
- [21] Wisconsin construction specification 3. Earthfill.
- [22] O'Neill MW, Murchison JM. An evaluation of py relationships in sands. University of Houston; 1983.
- [23] Wood LC. A review of digital pass filtering. *Reviews of Geophysics* 1968;6:73–97.
- [24] Youngworth RN, Gallagher BB, Stamper BL. An overview of power spectral density (PSD) calculations. *Optical Manufacturing and Testing VI* 2005;5869:206–16